PHOSPHOR THERMOMETRY USING RARE-EARTH DOPED MATERIALS

By

Rachael A. Hansel

Dissertation Proposal

Submitted to the Faculty of the

Graduate School of Vanderbilt University

in partial fulfillment of the requirements

for the degree of

DOCTOR OF PHILOSOPHY

in

Interdisciplinary Materials Science

December, 2010

Nashville, Tennessee

Approved:

Professor D. Greg Walker

Professor Charles Lukehart

Professor Tim Hanusa

Professor Richard Haglund

Dr. Steve W. Allison

TABLE OF CONTENTS

Page

LIST OF FIGURES

LIST OF TABLES

CHAPTER I

INTRODUCTION

Thermometry Devices

Accurate, reliable, temperature measurement is vital to the success of virtually every field in science and engineering. There are many devices readily available for temperature sensing. However, each method is best suited for certain applications.

Thermocouples, for example, are composed of two wires of dissimilar metals. The junction between the two metals produces a voltage that is proportional to the temperature of a surface in direct contact with the device. Thermocouples can accurately measure temperatures up to approximately 2500 °C (±1 °C depending on the metals) (9). However, exposing thermocouples to oxidizing or reducing environments, such as in gas turbine engines, can damage the metals. Also, non-stationary surfaces, such as turbine blades or pistons, cannot be measured because thermocouples require direct, physical contact with a surface. Likewise, the presence of a thermocouple on a surface can be disruptive to the fluid dynamics of a given system.

Rotating and other non-stationary surface temperatures can be measured using a non-contact technique such as thermal paints or liquid crystals. The chemical structure of these thermally-responsive materials changes in proportion to temperature changes. Thermal paints can measure temperatures up to 1270 °C with ± 1 °C accuracy (9). However, these materials are also not durable in combustion or abrasive environments.

Non-contact, optical temperature-measurement techniques, such as pyrometers, have been used in harsh environments. Pyrometers measure blackbody radiation which is naturally radiated from objects above absolute zero. Blackbody radiation is focused onto the detector that converts the measured wavelength to temperature. However, the temperature

detected is dependent on the energy emitting characteristics of different materials or the emissivity of the material. Consequently, the emissivity of an object may change with time as its surface corrodes or oxidizes. Pyrometers are also sensitive to other sources of incident radiation, such as nearby hot objects or stray light. (9)

Phosphor thermometry is another non-contact technique that uses optical signals to measure temperature remotely. However, this technique is not vulnerable to the issues of pyrometers, thermocouples, thermal paints, and many other thermal sensors. Phosphors are composed of a ceramic lattice doped with a small amount of luminescent ions and will emit visible, infrared, or UV radiation upon excitation from an external energy source. The intensity, wavelength, or lifetime (duration of light) of the visible emission is used to determine the temperature of a surface. Unlike many other thermocouples and thermal paints, phosphors are composed of inorganic, ceramic materials which means that phosphors are resistant to oxidation in high-temperature environments and are non-reactive with harsh chemicals. Phosphors are non-intrusive to the flow of liquids because the phosphor powder can be uniformly coated on a surface using electron beam pulsed vapor deposition (EBPVD) or atomic plasma spray (APS). The visible radiation of some phosphors has a narrow bandwidth ($\pm$5 nm) which eliminates interference from blackbody radiation. Measurements are comparable in accuracy compared to other thermometry devices and currently, temperatures can be measured up to 1500 $^{\circ}$C (2).

Table 1.1 summarizes the differences between the aforementioned thermometry methods.

Thermographic Phosphors

Phosphors that have been specifically designed for non-contact temperature measurement are called *Thermographic Phosphors* (TGPs). These materials consist of an oxide matrix and are doped with a rare-earth (RE) or transition metal ion. TGPs are excited with an energy source such as an electron beam, UV light, or a voltage source, and the emitted

luminescence can be in the UV, visible, or even in the infrared region. In this work, we will focus on RE-doped phosphors that emit in the visible region.

Several researchers have shown that phosphors can be used in a variety of applications. For example, (10) have used laser-induced fluorescence of a thermographic phosphor to measure the surface temperature of the rotor in an operating permanent-magnet motor. Also, (11) has shown that phosphors can be combined with thermal barrier coating materials to monitor surface temperatures of turbine blades. (12) has shown that chromium-doped phosphors can be used in biomedical thermometers. (13) used emission of europium-doped YVO_4 to determine the temperature of microparticles in a plasma flame. The reader is referred to an excellent review by (2) for a comprehensive overview of all the potential applications of thermometry devices phosphors.

Measurement Methods

Phosphors can be used as thermometers because higher temperatures cause radiative energy to be emitted as heat or lattice vibrations. These non-radiative transitions are strongly dependent on temperature and can drastically affect photoluminescent properties such as the luminescence wavelength, intensity, or lifetime. Surface temperature measurements are determined by evaluating experimental luminescent data against calibration data, which contain the temperature-dependence of a particular luminescent property. Surface temperatures can be obtained by evaluating the emission wavelength, intensity, or the lifetime (duration of the emission). In this work, we will focus on detecting the temperature-dependent lifetime.

Line Shift Method

The peak of the emission wavelength for some phosphors changes as a function of temperature. For example, the peak emission wavelength of ZnO : Ga at room temperature

is approximately 390 nm. As the temperature increases to 700 °C , the emission wavelength shifts to 480 nm (See Figure 1.1). (1) have shown that this method can be used to determine the temperature of particles in a flow. (The additional peak at 450 nm at 954 K, has been attributed to the excitons localized on donors and excitons bound with optical phonons. (14))

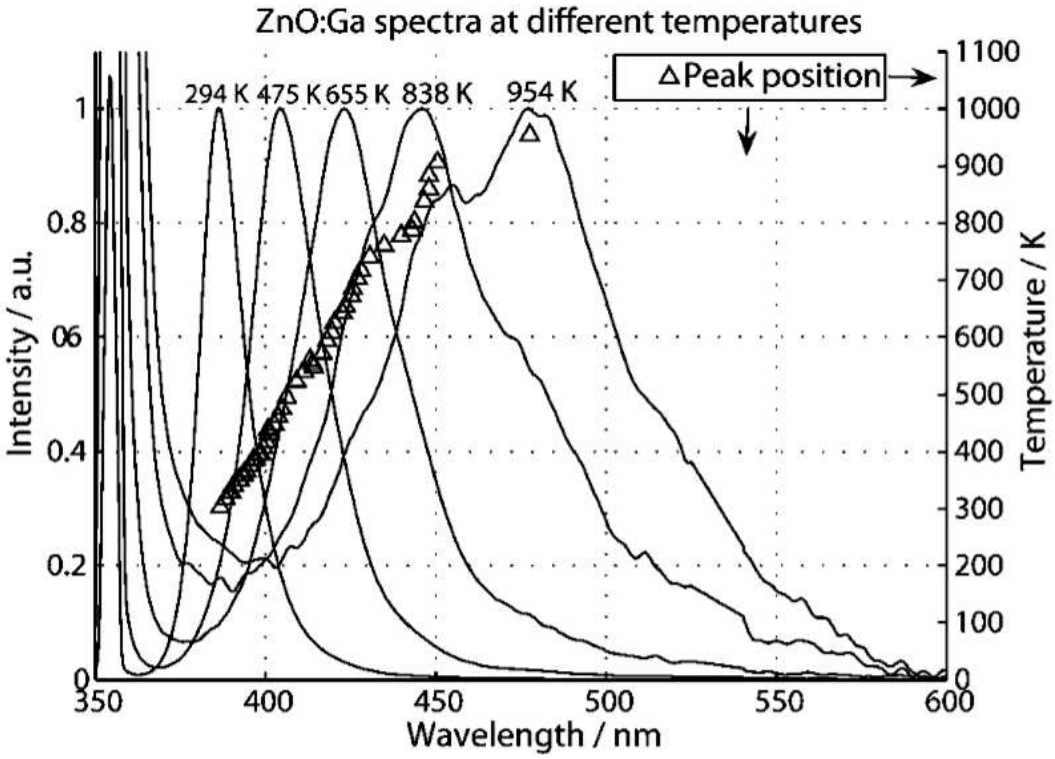

Figure 1.1 ZnO:Ga spectra showing red-shift as temperature increases. (1)

Relative Emission Peak Intensity

The relative intensity of an emission peak can be used to determine surface temperatures. Andrew Heyes of Imperial College in the UK has shown that the relative intensities of the blue emission lines change as a function of temperature in yttria-stabilized zirconia

(YSZ) doped with dysprosium (Figure 1.2). The intensity of the transition at 456 nm increases with temperature, while the intensity of the transition at 482 nm remains relatively constant.

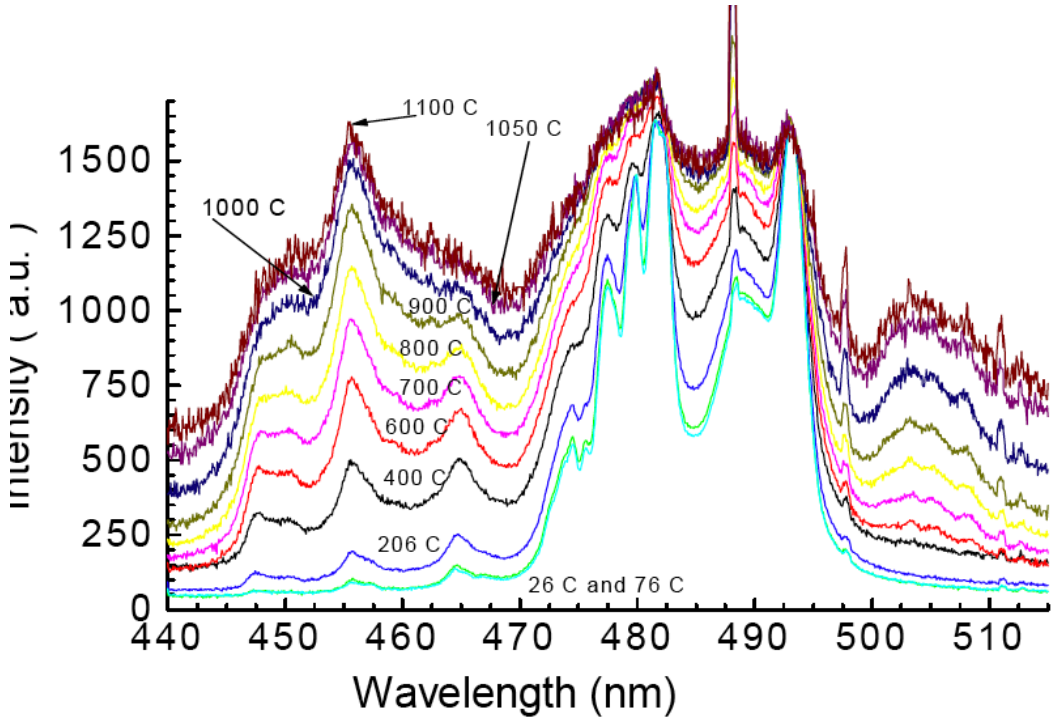

Figure 1.2 YSZ:Dy spectra showing relative intensity change as a function of temperature. Source: Communication with Andrew Heyes of Imperial College

Lifetime Measurement

The most common method used to determine the temperature of a surface is the luminescent lifetime. Upon excitation, fluorescence will be observed only if the source wavelength is shorter than the emitted fluorescence. The luminescence intensity decays

exponentially according to the relation:

$$I = I_o e^{-t/\tau}$$

where I is the intensity, I_o is the initial intensity, t is the time, and τ is the decay time constant. For most phosphors, the decay time is relatively constant at low temperatures and becomes temperature sensitive as the temperature increases. The calibration curves of selected phosphors are shown in Figure 1.3. The point at which the lifetime begins to decrease as a function of temperature is called the quenching temperature. For example, the lifetime of YAG:Dy is constant from 0-1100 °C . At approximately 1100 °C (the quenching temperature) the lifetime begins to decrease with temperature. The temperature range for which YAG:Dy would be useful as a sensor is between 1100-1400 °C .

The temperature dependence of the lifetime arises from the probability of each state being occupied at different temperatures. The number of non-radiative transitions increases at high temperatures compared to lower temperatures. Therefore, decay times are much shorter at high temperatures since more of the luminescent energy is being converted to phonon emission instead of luminescent energy. This project will focus on utilizing the decay time to determine surface temperatures.

Challenges and Objectives

One of the main challenges facing the field of phosphor thermometry is the lack of understanding of the physical mechanisms determining the transitions between electronic levels of both the host lattice and the luminescent dopant ion. Most TGP materials were developed for lighting applications where the operating temperature of the material remains relatively low and constant. As a result, there is limited information in the literature about luminescence of materials at temperatures greater than 300°C. Further, theoretical understanding of non-radiative process at elevated temperatures remains limited and un-

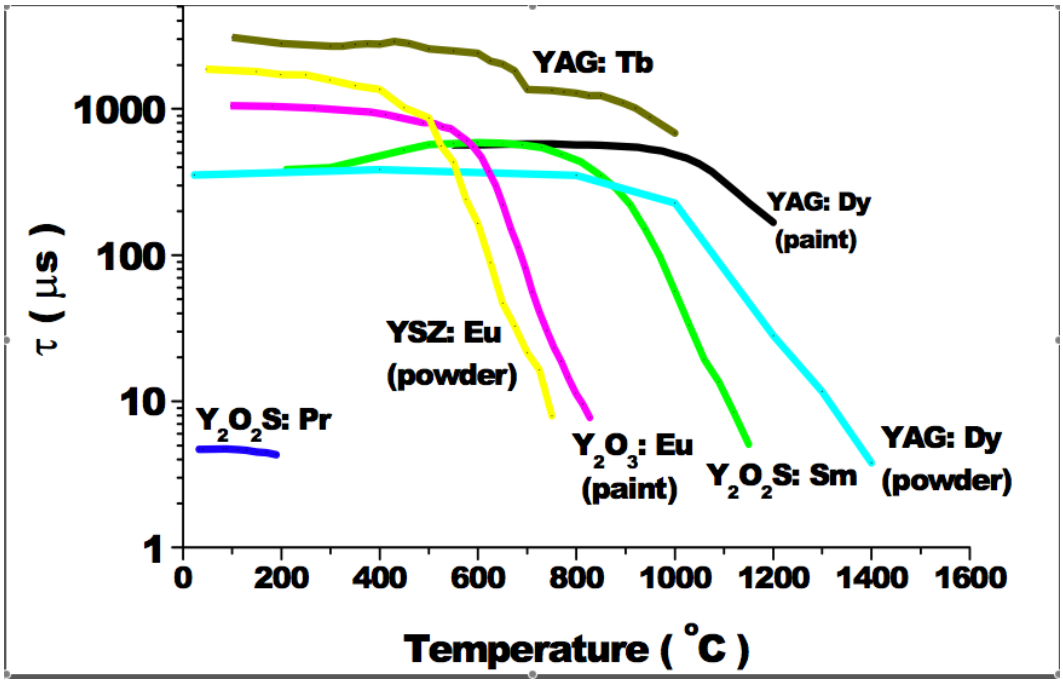

Figure 1.3 Lifetime versus temperature of selected phosphors. (2)

clear. Theoretical models describing thermal quenching have been proposed since the early 1970's. (4) proposed the quantum mechanical single configurational coordinate model (QMSCC) in 1975, which adequately described the luminescence quenching of trivalent chromium in Al_2O_3 at different temperatures. Other explanations, such as multi-phonon emission (MPE) theory, have been used to successfully predict trends in thermal quenching temperatures for a series of phosphors (15). However, MPE theory predicts unrealistic temperatures for some europium-doped phosphors (16).

Another related challenge is the issue of trying to find other phosphor materials that can be used as temperature sensors at temperatures greater than 1500 °C . Research on some pyrochlore materials has shown promise in recent years. (17) showed that $Eu_2Zr_2O_7$ can be used as a TGP up to 1200 °C . (6) have shown that $La_{1.92}Eu_{0.08}Zr_2O_7$ and $La_{1.92}Eu_{0.08}Hf_2O_7$ will emit visible radiation until about 700 °C . One of the goals of the proposed work is to re-examine the calibration curves of these pyrochlores using another excitation wavelength.

The two main goals of the proposed work are 1) to calculate the lifetimes of two different groups of materials (garnets and pyrochlores) using the QMSCC model and 2) to determine if a group of pyrochlore materials can be used for high-temperature applications. To accomplish the first goal, input parameters will be obtained from spectral data for use in a simple calculation to determine the fluorescent lifetime as function of temperature. The second goal will be accomplished by re-examining the calibration curve of some previously used pyrochlore materials with different excitation wavelengths. The results of this work will aid in the design of thermographic phosphors for high-temperature applications.

Table 1.1 High-Temperature Measurement Techniques

Method	Temperature Range (°C)	Applications	Advantages	Disadvantages
Thermocouples	-250 - 2320	• steel industry • furnaces • chemical processing plants	• inexpensive materials • wide temperature range	• disrupts flow patterns • not chemically stable in all environments • low accuracy • unuasble on rotating surfaces
Thermal Paints	48- 1250	• food safety/ monitoring • medical applications • clothing • high speed flight technology	• can measure moving parts • inexpensive installation • fast reaction time	• can be environmentally intrusive • not stable in corrosive environments • poor resolution/low accuracy
Pyrometry	196 -1250	• non-stationary surfaces • smelting industry	• fast response time • wide temperature range • inexpensive	• optical access required • sensitivity to stray light • sensitivity to emissivity variation • sensitive to interference with dust, gas, and particulate matter • sensitivity to stray light (i.e. flames in combustion engines)
Phosphor Thermometry	0 - 1500	• turbine engines • biomedical uses • Optical fiber fluorescence	• chemical stability in most atmospheres • no contact required for measurement • can measure moving parts • fast reaction • non-intrusive measurements	• optical access required • weak signal at high temperatures • limited theoretical understanding of non-radiative transitions

CHAPTER II

THEORY

There are several model systems that can be used to calculate non-radiative decay. (18) systematically studied multiphonon emission (MPE) in several rare-earth doped crystals. Multiphonon emission involves the simultaneous emission of several phonons from one state to another and has been used to account for non-radiative decay of luminescence. This simple model works well for transitions between states with low energy differences (i.e. requiring the spontaneous emission of less than 5-10 phonons). However, MPE emission does not accurately describe transitions between states with large energy gaps, such as in Eu^{3+} (16) (6). Engleman has explicitly derives the hamiltonian that governs both radiative and non-radiative transitions (19).

The majority model electronic transitions in a configurational one-dimensional space. The assumption is that electronic motion depends on one type of ionic displacement. This one-dimensional displacement is referred to as the interaction coordinate and describes a physical distance between two nuclei.

The single configurational coordinate (SCC) model of Struck and Fonger predicts non-radiative decay by considering states to be in thermal equilibrium and using the Manneback recursion formulas to calculate the overlap integrals (4). A sample configurational coordinate diagram is given Figure 2.1. The parabola u and v are the ground and excited state potential energy wells, respectively. The vibrational wavefunctions are u_n and v_m. The phonon energies for each parabola are $\hbar\omega_u$ and $\hbar\omega_v$, respectively. The distance between the equilibrium distance of each parabola is measured by the Frank-Condon offset, a_{uv}. The assumption is that electronic motion depends on only one type of ionic displacement. The parabola offset is expressed in terms of S_u and S_v such as, $a_{uv}^2 = 2(S_v + S_u)$. The relaxation

energy after emission and absorption are $S_u\hbar\omega_u$ and $S_v\hbar\omega_u$, respectively.

The u and v parabola represent the energy states of the two nuclei. The shape of the function is parabolic and follows from the motion of a simple harmonic oscillator.

$$E(Q) = \frac{1}{2}k(Q - a_{uv})^2 \tag{2.1}$$

The vibrational wavefunctions, v_m and u_n, for these energy states are defined anharmonically as

$$\psi_{n'}(Q) = N' e^{-\frac{1}{2}\eta^2} H_{n'}(\eta) \tag{2.2}$$

$$\psi_{n''}(Q) = N'' e^{-\frac{1}{2}\zeta^2} H_{n''}(\zeta) \tag{2.3}$$

where $\psi_{n''}(R)$, and $\psi_{n'}(R)$ are the normalized corresponding vibrational eigenfunctions and N is the normalization factor.

The reduced lengths, η and ζ, are defined as

$$\eta = \frac{Q - a_{uv}}{\rho'} \tag{2.4}$$

$$\zeta = \frac{Q - a_{uv}}{\rho''} \tag{2.5}$$

where the unit of length is $\rho = [h/4\pi^2\mu\nu']$. The unit of length physically means the displacement of a classical vibrator with a total energy of $h\nu'/2$ vibrating at frequency ν' with a reduced mass μ. The hermite polynomials, $H_{n'}$ and $H_{n''}$, are defined by the generating function and give rise to the eigenstates of the harmonic oscillator. (20)

According to the Franck-Condon principle, transitions between electronic states occur vertically. That is, a transition to a higher energy state occurs when the atomic distance is the same in both the lower and higher energy state. Equally, transitions are most

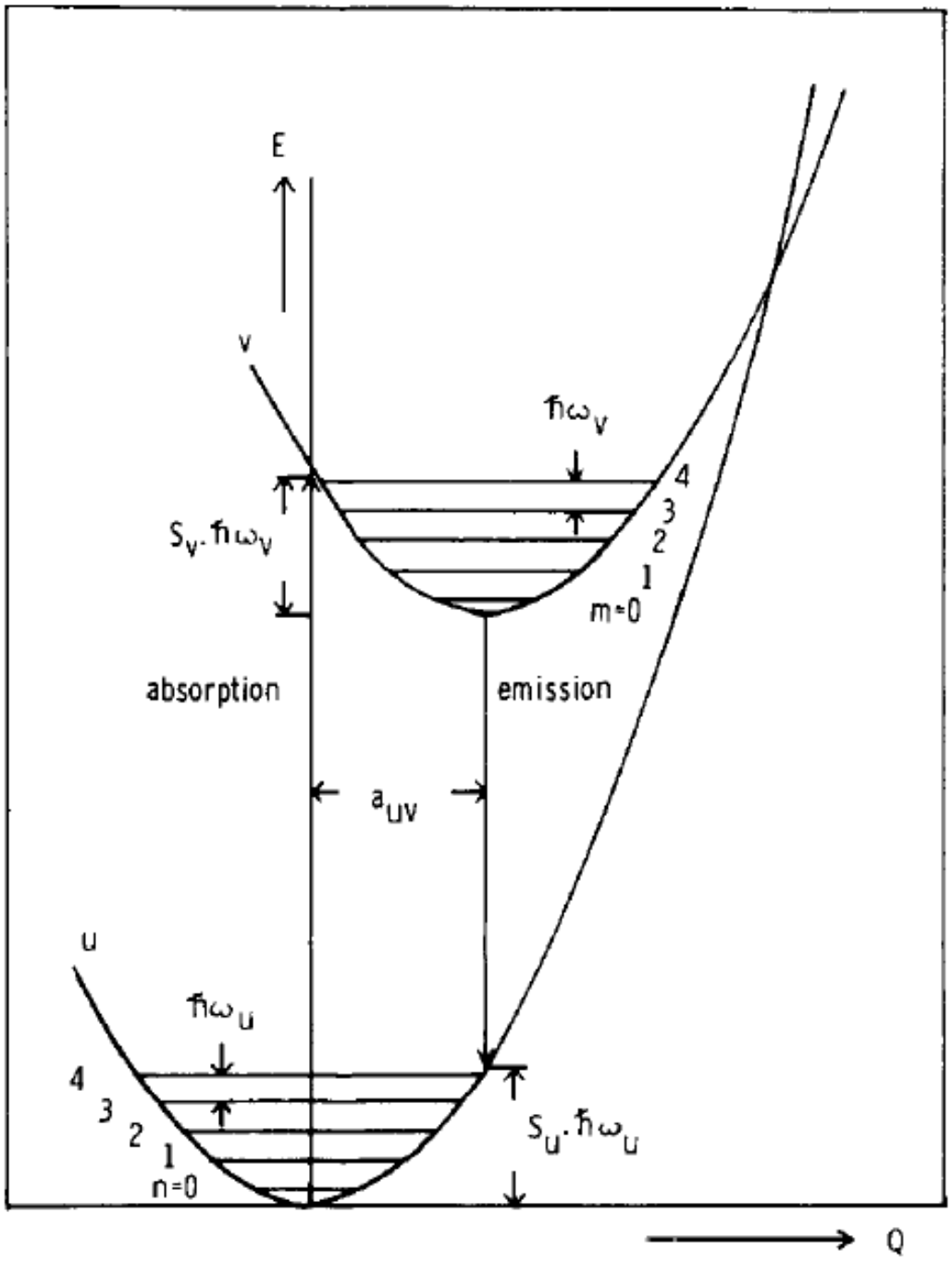

Figure 2.1 Configurational coordinate diagram Reference: [(3)]

likely to occur when the position and momentum of the nuclei are the same before and after the transition (21). The probability of the transition between electronic states is referred to as the transition moment and is described by Condon's overlap integral

$$C(m,n) = \int_0^\infty \psi_m(Q)\psi_n(Q)dQ \tag{2.6}$$

where Q is the nuclear separation (the configurational coordinate in the QMSCC), m is the vibrational quantum number in the higher-energy state, n is the vibrational quantum number of the lower energy state. Manneback et al. have evaluated Equation 2.6 by recursion formulas

$$A_{00} = (sin(2\theta))^{1/2} exp(-\frac{1}{8}(sin(2\theta))^2 a_{uv}^2 t) \tag{2.7}$$

$$(m+1)^{\frac{1}{2}} A_{n,m+1} = -cos(2\theta)m^{\frac{1}{2}}A_{n,m-1} - sin(2\theta)2^{-\frac{1}{2}}a_{uv}cos(\theta)A_{nm} + sin(2\theta)n^{\frac{1}{2}}A_{n-1,m} \tag{2.8}$$

$$(n+1)^{\frac{1}{2}} A_{n+1,m} = cos(2\theta)n^{\frac{1}{2}}A_{n-1,m} + sin(2\theta)2^{-\frac{1}{2}}a_{uv}sin(\theta)A_{nm} + sin(2\theta)m^{\frac{1}{2}}A_{n,m-1} \tag{2.9}$$

where a_{uv} is the difference in equilibrium distance between the two states. The angle θ is the ratio of the parabola force constants and phonon energies $(tan(\theta))^4 = k_v/k_u$. For equal force constants $\theta = 45^\circ$ (20)

The Franck-Condon factor, $C(m,n)$, in equation 2.6 (A_{nm} in equations 2.8, 2.9) describes the probability of a transition occurring based on the displacement of the parabolas, the relative energy difference between the states, and the phonon frequencies of the parabolas. In this work, the phonon frequencies of the excited and ground states are assumed to be equal. That is, $\theta = 45^\circ$ because $\bar{h}\omega_u = \bar{h}\omega_v$.

After the electron is promoted to a higher energy state, the atoms are not in equilibrium position. The atoms will move to the equilibrium position of the new electronic state in about $10^{13}s^{-1}$-$10^{12}s^{-1}$ The excess energy is given off in the form of lattice vibrations and the transitions are non-radiative. In contrast, a radiative transition is much slower; on the order of $10^2 s^{-1}$.

Thermal quenching of emission occurs by energy being released in the form of photons or phonons by competing non-radiative and radiative pathways. The QMSCC model assumes that the vibrational states are in thermal equilibrium and that the $v_m \rightarrow u_n$ rate is proportional to the square of the overlap integral $< u_n|v_m >^2$. The overlap integral is A_{nm} in equations 2.8 and 2.9.

Therefore, the radiative rate, R_{nm}, and non-radiative rate, N_{nm} are

$$R_{nm} = R_{uv}(1-r_v){r_v}^m < u_n|v_m >^2 \tag{2.10}$$

$$N_{nm} = N_{uv}(1-r_v){r_v}^m < u_n|v_m >^2 \tag{2.11}$$

where $r_v = exp(-\bar{h}\omega/kT)$. All calculations in this work consider the phonon frequencies of each state to be equal. That is, $\bar{h}\omega_u = \bar{h}\omega_v$. The radiative constant, R_{uv}, is considered a constant that is chosen empirically. The non-radiative constant is approximated as $10^{13}s^{-1}$. Both R_{uv} and N_{uv} are derived from the electronic portion of the transition integral. The thermal weights are $(1-r_v){r_v}^m$. These weights give the thermal average of the quantity for the quantum index m and are normalized such that

$$W_m = \sum_{m=0}^{\infty}(1-r_v){r_v}^m = 1 \tag{2.12}$$

The radiative and non-radiative energy balances are

$$h\nu_{zp,vu} + m\bar{h}\omega_v - n\bar{h}\omega_u + h\nu_{nm} = 0 \tag{2.13}$$

$$h\nu_{zp,vu} + m\bar{h}\omega_v - n\bar{h}\omega_u = 0 \tag{2.14}$$

respectively, where the zero-phonon energy is $h\nu_{zp,vu}$, which is the energy difference between $v_{m=0}$ and $u_{n=0}$. The photon energy of absorption and emission is $+h\nu_{nm}$ and $-h\nu_{nm}$, respectively.

The radiative constant, R_{uv}, is a considered to be a constant from the electronic portion of the transition integral and is approximated as $10^2 s^{-1}$ for forbidden transitions, but can be $10^7 s^{-1}$ for permitted electric dipole transitions (4). The thermal weights are summed to unity so the $\sum_{n,m=0}^{\infty} R_{nm} \approx R_{uv}$ and R_{uv} is the temperature-independent radiative rate. The non-radiative electronic factor, N_{uv}, is also considered a constant from the electronic portion of the integral and is empirically chosen as $\approx 10^{13} s^{-1}$. The non-radiative transition rate is determined by summing over all nearly resonant v_m and u_n states that satisfy the energy balance in Equation 2.14. The total non-radiative rate can dominate the radiative rate because the non-radiative constant is so much larger than R_{uv}. Furthermore, the total non-radiative transition rate $\sum_{m=0}^{\infty} N_{nm}$ increases with temperature which causes the quenching of radiative emission.

All radiative transitions that have the same energy difference are grouped together by a single quantum number, $p_U \equiv n - m$. All radiative transitions with the same p_U have the same photon energy $h\nu_{p_U}$:

$$h\nu_{zp,vu} - pU\bar{h}\omega_0 + h\nu_{nm} = 0 \tag{2.15}$$

with $\bar{h}\omega_0 = \bar{h}\omega_u = \bar{h}\omega_v$ because $\theta = 45^\circ$. For the linear coupling case ($\theta = 45^\circ$), the summed thermal Franck-Condon weight is

$$U_{pU} = \sum_{m=m_0}^{\infty} (1 - r_v) {r_v}^m < u_{pU+m} | v_m >^2 \tag{2.16}$$

where $m_0 = 0$ for $p_U \geq 0$. Therefore, the radiative and non-radiative transition rates for $(v \rightarrow u)$ transitions, indexed by p_U are

$$R_{pUv} = R_{uv} U_{p_U} \tag{2.17}$$

$$N_{pUv} = N_{uv} U_{p_U} \tag{2.18}$$

The temperature-dependent band shape is obtained from the normalized distribution of U_{p_U} in Equation 2.16. The QMSCC model predicts emission quenching of luminescent materials as a function of temperature. Emission quenching is a result of non-radiative transitions (NRT). NRTs are highly dependent on temperature and compete with radiative energy release. Thus, thermal quenching of radiative emission can be explained within the context of the configurational coordinate model. Figure 2.1 shows an example of ($v \rightarrow u$) transitions for states with a large parabola offset. Upon excitation into the v state, energy is released to the ground state by two competitive process: 1)radiative emission from the lowest vibrational level of v to u and 2) by releasing energy non-radiatively by thermal activation from v into the high levels of g. The ($v \rightarrow u$) crossover is a non-radiative transition. Therefore, the total non-radiative rate is $N_{uv}U_{p_u}$, where $N_{uv} = 10^{13}s^{-1}$ and U_{p_u} is the summed thermal weights for the transition between v and u. The total radiative transition rate from v to u is R_{uv}. The quantum efficiency of the ($v \rightarrow u$) transition is the total radiative rate divided by all possible radiative and non-radiative transitions

$$\eta_{gv} = \frac{R_{uv}}{R_{uv} + N_{uv}U_{p_u}} = \frac{1}{1 + (N_{uv}/R_{uv})\,U_{p_u}} \tag{2.19}$$

The lifetime of the v state is the inverse of the sum of all non-radiative and radiative transitions and can be expressed as

$$\tau_v = \left(\frac{1}{\sum R_{nm}} + \frac{1}{\sum N_{nm}}\right) = \frac{1}{R_{uv} + N_{uv}U_{p_u}} \tag{2.20}$$

In other systems, there are often multiple states that can contribute to thermal quenching of emission. Figure 2.2 shows the configurational coordinate diagram with several electronic states. The u and t states are low in energy compared to the v state. The high energetic location of the v state represents the charge transfer state found in Eu^{3+} and other lanthanoid ions and can significantly affect emission quenching. (The charge transfer state is described in more detail in the following chapters.) The offset between the u, t, and

g states is very small compared to the offset between g and v. Upon excitation into the v-state, energy can be released to the ground states through a number of competing radiative and non-radiative pathways.

Energy is most likely released from the bottom of the energy parabola, that is when $m = 0$ in v. The energy can be released radiatively from point B to g. However, energy can also be released non-radiatively from the lowest vibrational level of v to high vibrational levels of u or t. Consequently, the v-state feeds rapidly into the u and t state because the u and t state intersect near the minima of the v-state.

Excitation into the u-state can result in either a non-radiative transition to the t-state and then a radiative $t \rightarrow g$ transition (i.e. $u \rightarrow v \rightarrow t$) or a single non-radiative $u \rightarrow t$ transition and then the radiative $t \rightarrow g$ (i.e. $u \rightarrow t \rightarrow g$) . The non-radiative transitions in Figure 2.2 are $(v \rightarrow u)$, $(u \rightarrow t)$, $(v \rightarrow t)$, and $(v \rightarrow g)$. The radiative transitions are $(u \rightarrow g)$, $(t \rightarrow g)$, and $(v \rightarrow g)$.

All possible transitions must be considered in order to calculate the total radiative and non-radiative rates. For example, in order to calculate the quantum efficiency and lifetime of $u \rightarrow g$ emission the total rate leaving u and v for g and t is

$$\Sigma = (u \rightarrow g,t)n_u + (v \rightarrow g,t)n_v \tag{2.21}$$

where n_u and n_v are the populations for the u and v states, respectively. The derivation of the temperature-dependent lifetime was derived in the same manner as (4). The quantum efficiency is determined by multiplying the rate for the $u \rightarrow g$ transition by the population of the u state and then dividing by the total rate in Equation 2.21

$$\eta_{gu} = \frac{(u \rightarrow g)n_u}{\Sigma} = \frac{(u \rightarrow g)n_u}{(u \rightarrow g,t)n_u + (v \rightarrow g,t)n_v} = \left\{1 + \frac{(u \rightarrow t)}{(u \rightarrow g)} + \frac{(v \rightarrow g,t)}{(u \rightarrow g)}\frac{n_v}{n_u}\right\}^{-1} \tag{2.22}$$

The population ratio n_v/n_u ca be defined by utilizing the steady-state equilibrium equations

$$(u \rightarrow g,t), n_u - (v \rightarrow u)n_v = G_u \tag{2.23}$$

$$(v \rightarrow g,t,u), n_v - (v \rightarrow u)n_u = G_v \tag{2.24}$$

where G_u and G_v are the excitation rates into the u and v states, respectively. For excitation into u, $G_v = 0$. For excitation into v, $G_u = 0$. Thus, the population ratio can be defined as

$$\left.\frac{n_u}{n_v}\right|_{G_u=0} = \frac{(u \rightarrow v)}{(v \rightarrow g,t,u)} \tag{2.25}$$

$$\left.\frac{n_u}{n_v}\right|_{G_v=0} = \frac{(v \rightarrow g,t,u)}{(v \rightarrow u)} \tag{2.26}$$

The quantum efficiency is determined by substituting Equations 2.25 and 2.26 into Equation 2.22.

$$\eta_{gu}|_{G_v=0} = \left\{1 + \frac{(u \rightarrow t)}{(u \rightarrow g)} + \frac{(v \rightarrow g,t)(v \rightarrow u)}{(u \rightarrow g)(v \rightarrow g,t,u)} r_0^{pU}\right\}^{-1} \tag{2.27}$$

where $r_0^{pU} = (u \rightarrow v)/(v \rightarrow u)$. The lifetime is defined by excitation into u ($G_v = 0$)

$$\tau_u = \left.\frac{n_u + n_v}{(u \rightarrow g,t)n_u + (v \rightarrow g,t)n_v}\right|_{G_u} = \frac{n_u + n_v}{(u \rightarrow g)n_u}\eta_{gu}|G_u = \frac{1}{(u \rightarrow g)}\left(1 + \frac{n_v}{n_u}\right)\eta_{gu}|G_u \tag{2.28}$$

A detailed calculation of two measured systems is presented in subsequent chapters. All calculations in this work were performed using scripts for Matlab. The calculation of the overlap integrals requires the most work. The total time for calculation of the lifetime was approximately 5 minutes.

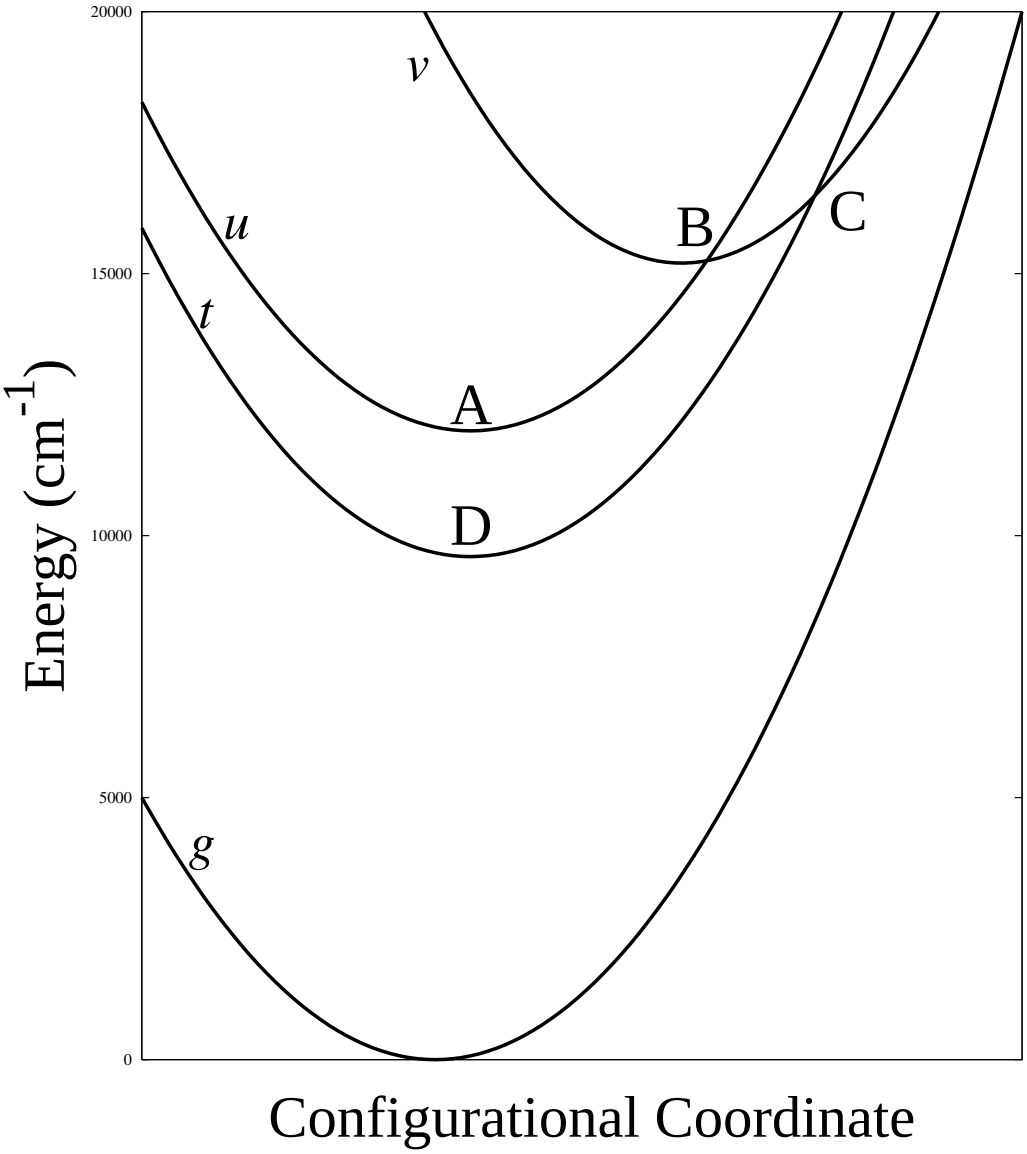

Figure 2.2 Configurational coordinate diagram showing multiple states adapted from Figure 8 in (4)

Rare Earth Electronic States

The transition rates between electronic states govern the temperature-dependent optical properties of the phosphor material. The electronic states of the rare-earth elements are numerous and energetic values vary widely for each element. The relative positions of the rare-earth energy levels have been determined by Dieke and his co-workers at John's Hopkins University (5) . The "Dieke diagram", shown in Figure 2.3, shows the energy levels for trivalent lanthanide ions as a function of the number of electrons in the 4f shell, *n*. The electronic states are denoted by a set of quantum numbers, which use the Russel-Saunders notation

$$^{2S+1}L_J \tag{2.29}$$

where *S* represents the spin angular momentum and is equal to the number of unpaired electrons divided by 2. The total orbital angular momentum is *L*.

Optical transitions between the 4f states of the rare-earth elements are normally forbidden due to the parity selection rule (22). However, the parity selection rule is relaxed when the rare-earth ion occupies a crystal lattice site. Opposite-parity wavefunctions of the 5d orbitals of the host lattice, for example, mix with the 4f wavefunctions. As a result, 4f-4f transitions are observed. The arrows between the electronic states in Figure 2.3 indicate the most commonly observed radiative transitions. However, non-radiative transitions between the 4f-4f states and the 4f-host lattice states are strongly dependent on temperature and significantly affect the optical properties. Although the 4f states are well-shielded from outer orbitals, the electronic orbitals of the host lattice can affect the optical properties of the materials. The temperature-dependence of the non-radiative transitions is the reason that phosphors can be used as temperature sensors. One of the main goals of this work is to enhance the physical understanding of the physical mechanisms dictating both radiative and non-radiative phosphor transitions.

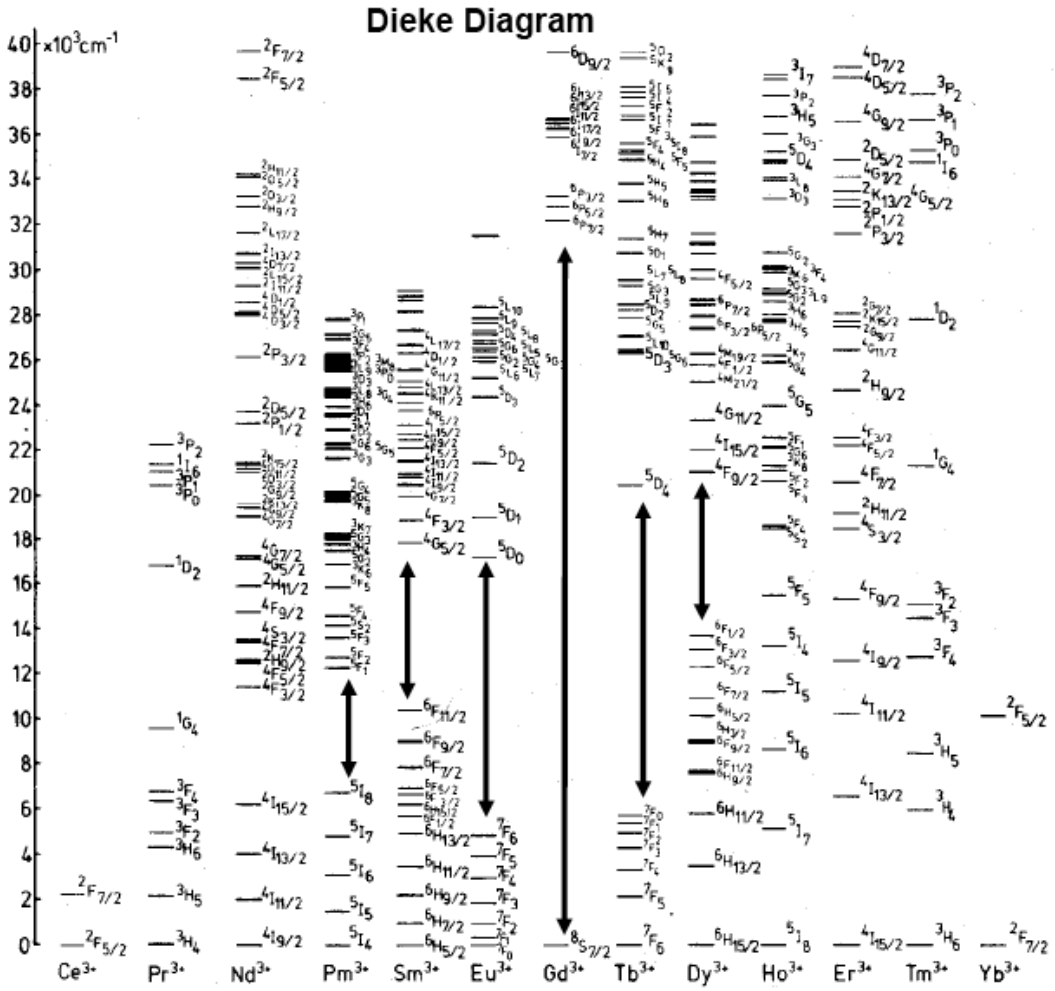

Figure 2.3 Rare-earth energy levels or the ”Dieke Diagram” (5)

Input Parameters

The input parameters needed to calculate the QMSCC model are the parabola force constant, θ, the parabola offset, a_{uv}, and the relative energy differences between the electronic states. These parameters are needed primarily to calculate the Manneback recursion formulas that give the overlap integrals of Equation 2.6.

The parabola offset, a_{uv}, is determined from excitation and emission spectra. In the QMSCC, this parameter measures the difference in equilibrium bond distance between atoms. Experimentally, this parameter can be determined from the geometrical relationship depicted in Figure 2.1, where

$$a_{uv}^2 = 2(S_u + S_v)$$

The relaxation energies after emission and absorption are $S_u\hbar\omega_u$ and $S_v\hbar\omega_v$, respectively. The energy differences between electronic states is also found from experimental spectroscopy data.

In this study, the parabola force constant of the excited and ground state is assumed to be similar. The parabola force constant is a measure of the strength between atoms. This assumption may not always represent the true physical system. However, Grinberg has shown that the variation of θ does not significantly improve the correlation of calculated and experimental data (23).

Chapter Summary

In the following chapters, we will use the QMSCC model to calculate the luminescent lifetime as a function of temperature for two groups of materials: cerium-doped garnets and europium-doped pyrochlores. These two groups of materials are representative of high- and low-temperature phosphors. The calculation for cerium-doped garnets will involve the transitions between the excited energy states of the 5d orbitals (d_1 and d_2) and the ground states of the 4f orbitals ($^7F_{5/2}$ and $^7F_{7/2}$) over a range of temperatures. In this

experiment we have altered the structure by atom-substitution and have observed how this structure variation affects the calibration curve. The calculations for the europium-doped pyrochlore materials will involve calculating the 4f-4f transitions ($^5D_{0-3}$ to $^7F_{1-6}$). Also, a high energy state called the charge transfer state (CTS) can also affect the transfer of energy to lower 4f levels and will be included in our calculations. The CTS represents the state of the bonding orbitals of the rare-earth and the neighboring oxygen atom. Energy absorbed by the 4f orbitals of Eu^{3+} can be thermally transfered to the CTS. Recent results have shown that pyrochlores are capable of being used as a sensor for high-temperature applications, such as combustion engines. All calculated results will be compared to previous experimental results.

CHAPTER III

PYROCHLORES

Introduction

Pyrochloric compounds are a group of inorganic ceramics under consideration for use as non-contact, temperature sensors. These materials are excellent candidates for high-temperature thermographic phosphors because the crystal structure is stable in high-temperature, oxidizing environments and because they emit intense, visible emission. For example, pyrochlore zirconates, $A_2Zr_2O_7$, can be used as thermal barrier coatings (TBC) because they exhibit a high coefficient of thermal expansion, a high melting point, and low thermal conductivity (24). Also, lanthanum pyrochlores, $La_2B_2O_7$, are hosts for Eu^{3+}-doping and exhibit intense visible luminescence (25). Furthermore, Gentleman has shown that Eu-doped Gd_2Zr_2O7 is sensitive to temperature at least up to 1200 °C (17).

The formula for pyrochlore compounds is $A_2B_2O_7$ (where A=Y, La, Nd, Sm, Eu, Gd; B=Ti, Zr, Hf, Sn) where the A and B atoms are in the $+3$ and $+4$ oxidation state, respectively (25). Several pyrochlores have lower thermal conductivity than the current TBC industry standard, yttria-stabilized zirconia (YSZ). One reason is because the stabilized pyrochlore structure is similar to the fluorite structure of YSZ. Large atoms in the A site, such as La^{3+}, stabilize the pyrochlore structure up to about 1500 °C . Lanthanum zirconates have been shown to have low thermal conductivities between 700-1200 °C (26). Co-doping on the A and B sites has also been suggested to improve thermal conductivity and modify the thermal expansion coefficient (26). The spectral properties can also be tuned by doping on both sites.

The intense red emission of Eu^{3+}-doped pyrochlores are of particular interest for white-light emitting diodes, panel displays, and fluorescent light bulbs (27). The most

notable features of the emission spectra are the spectral bands due to transitions between the $^5D_0$ excited states to the ^7F_J ground states (See Figure 2.3 in Chapter II). The relative intensity of each peak is strongly dependent on the surrounding environment of Eu^{3+} in the host lattice. In general, if the Eu^{3+} atom is in a site with inversion symmetry, the magnetic dipole transitions between 580-610 nm and 635-660 nm will dominate, because electric dipole transitions are parity forbidden. The selection rules are relaxed in a site with low or no inversion symmetry which allows the electric dipole transitions between 610-635 nm and 710 nm to increase in intensity (25). Emission spectra of pyrochlores reveals important structural information about the materials. Although the emissive properties of lanthanum pyrochlores have been well-studied, temperature-dependent spectral properties remain relatively unknown, especially for high-temperatures.

Recently, Gentleman obtained luminescent lifetime data as a function of temperature for several pyrochlore zirconates (17). (17) have demonstrated that the temperature-dependent luminescent lifetimes of $Gd_2Zr_2O_7$: Eu, $Sm_2Zr_2O_7$: Eu, and $Eu_2Zr_2O_7$ are sensitive to temperatures greater than 1000 °C . In this study, the temperature-dependent luminescent lifetime was determined for Eu^{3+} in two different pyrochlore lattices: $La_2Zr_2O_7$ and $La_2Hf_2O_7$. The substitution of the B site atom has been shown to cause a small, but significant effect in the structure which consequently affects the spectral properties. The temperature-dependent lifetime is compared to the calculations of the QMSCC model described in Chapter II.

Experimental

Samples of $La_{1.92}Eu_{0.08}B_2O_7$ where B = Zr^{4+} or Hf^{4+}, were made by the combustion of rare-earth nitrates with glycine (NH_2CH_2COOH) in a muffle furnace. Immediately following the auto-combustion, a voluminous, porous white powder formed. All samples were calcined in air for 2 hours at 1200 °C .

X-Ray Diffraction

The structure of the samples was determined by X-ray powder diffraction (XRD) patterns with CuKα ($\lambda = 1.5405$Å) radiation and are shown in Figure 3.1. Both spectra can be indexed to the Joint Committee on Powder Diffraction Standards (JCPDS) references (17-450 for $La_2Zr_2O_7$ and 37-1040 for $La_2Hf_2O_7$). The peaks at 28, 33, 48, and 56 correspond to the (222), (400), (440), and (622) planes of the pyrochlore structure, respectively. The spectra show that both samples are highly crystalline and single phase. (Note: The spectra for the pre-calcined samples were also highly crystalline; nevertheless, a slight decrease in intensity was observed.)

The lattice constant for $La_{1.92}Eu_{0.08}Hf_2O_7$ and $La_{1.92}Eu_{0.08}Zr_2O_7$ is 10.7 and 10.8 Å respectively. This small difference is caused by the difference in the radii of Hf^{4+} and Zr^{4+} (0.071nm and 0.072nm, respectively (28). In the pyrochlore structure, the A^{3+} ion is coordinated to eight non-equivalent oxygen atoms. Six of the oxygen atoms at a distance d_1 from the A^{3+} ion and the remaining two oxygens are at a distance, d_2, which is slightly shorter than d_1. (25) has shown that the difference between the ratio of d_1 to d_2 for the two lattices is only 0.8%.

Photoluminescence

Room-temperature photoluminescent spectra were taken using a Quantamaster 500 spectrometer. In this study, we are interested in using the intense emission at 611nm for temperature-dependent lifetime measurements. The excitation spectra is used to find the excitation wavelengths that will maximize the intensity of emission and also to discern important information about the host lattice effects on the orbitals of the Eu^{3+} ion. The excitation spectrum for $\lambda_{em} = 611$nm is shown in Figure 3.2. The broadband transition at 300nm is from the transition from the charge transfer state of the Eu-O bond to the ^7F_J ground states. The narrow-bands at 395, 460, 490, and 530 nm are due to transitions from

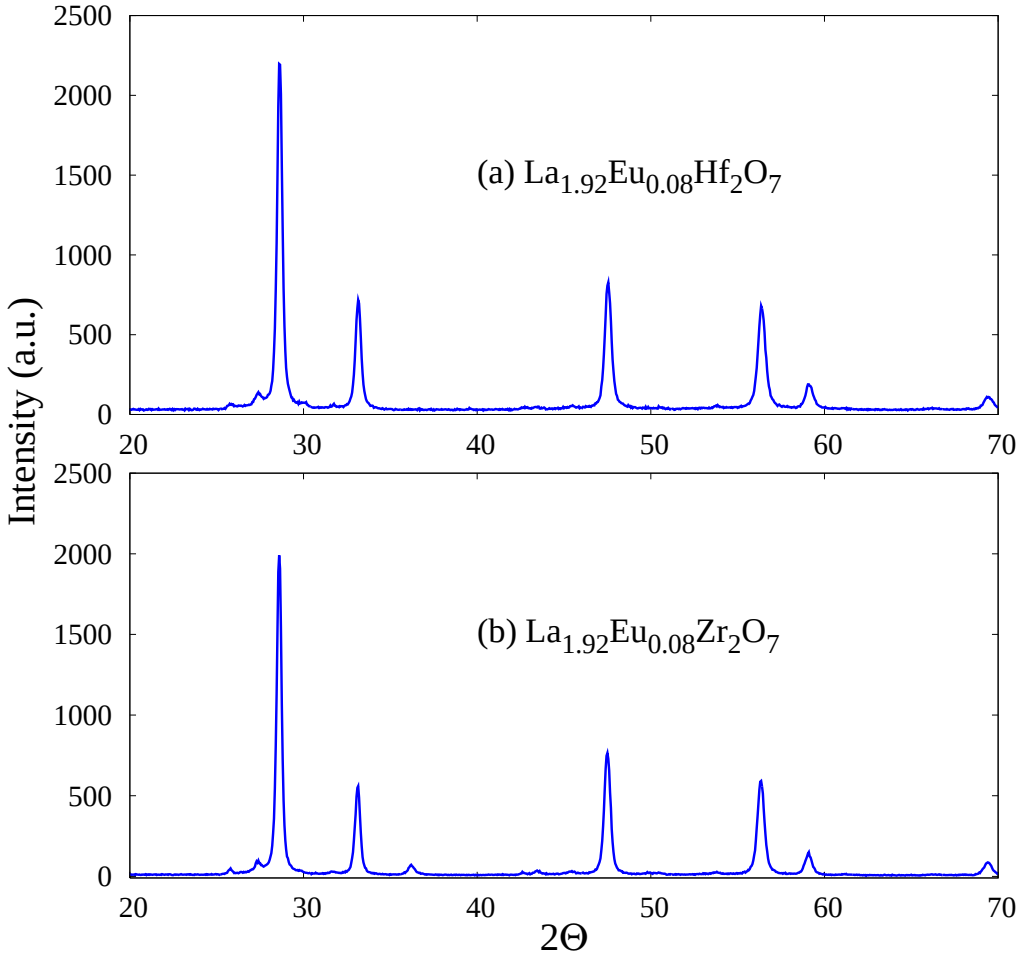

Figure 3.1 XRD patterns of $La_{1.92}Eu_{0.08}Zr_2O_7$ and $La_{1.92}Eu_{0.08}Hf_2O_7$

the $^5D_{0-3}$ states to the ground states. The peaks in Figure 3.2 indicate which wavelengths will produce the most intense emission at 611 nm. Excitation wavelengths of 337 nm and 532 nm were chosen for the temperature-dependent lifetime measurements.

The corresponding emission spectra for $\lambda_{exc} = 337$ nm and $\lambda_{exc} = 532$ nm are shown in Figure 3.3 and Figure 3.4, respectively. Transitions between 610-635 nm are caused by electronic dipole transitions between the $^5D_0 \rightarrow ^7F_2$ states. The emissions between 580-610 nm are due to magnetic dipole transitions between the $^5D_0 \rightarrow ^7 F_1$ states. Magnetic dipole transitions dominate when Eu^{3+} is located in a site with inversion symmetry. In contrast, electronic dipole transitions dominate when the luminescent ion is in a site without inversion symmetry. Therefore, the intensity ratio of $^5D_0 \rightarrow ^7 F_2$ to $^5D_0 \rightarrow ^7 F_1$ can be used to determine information about the site symmetry of the Eu^{3+} ion. From Figure 3.3 and Figure 3.4, it is obvious that electronic dipole transitions dominate since the red emission lines are the most intense.

Temperature-Dependent Lifetime

The experimental setup for the temperature-dependent lifetime measurements is shown in Figure 3.5. A nitrogen laser with an excitation wavelength of 337 nm was used to excite directly into the charge transfer state. For comparison, a separate experiment was performed using an YAG:Nd laser with $\lambda_{exc} = 532$ nm, which directly excites the lower $^5D_1$ state. A band-pass filter was used to collect only 611 nm light, which was the most intense emission band in Figures 3.3 and 3.4. Fiber optic cables were used to carry the excitation and emission light. Emission was detected by a photomultiplier tube. The phosphor sample was heated with a furnace and the temperature was externally monitored with a thermocouple. The lifetime of the red emission was determined as a function of temperature for $La_{1.92}Eu_{0.08}Hf_2O_7$ and $La_{1.92}Eu_{0.08}Zr_2O_7$.

The decay curves for both structures were multi-exponential and consisted of a slow and fast component. The sources of multi-exponential decay were not investigated in this

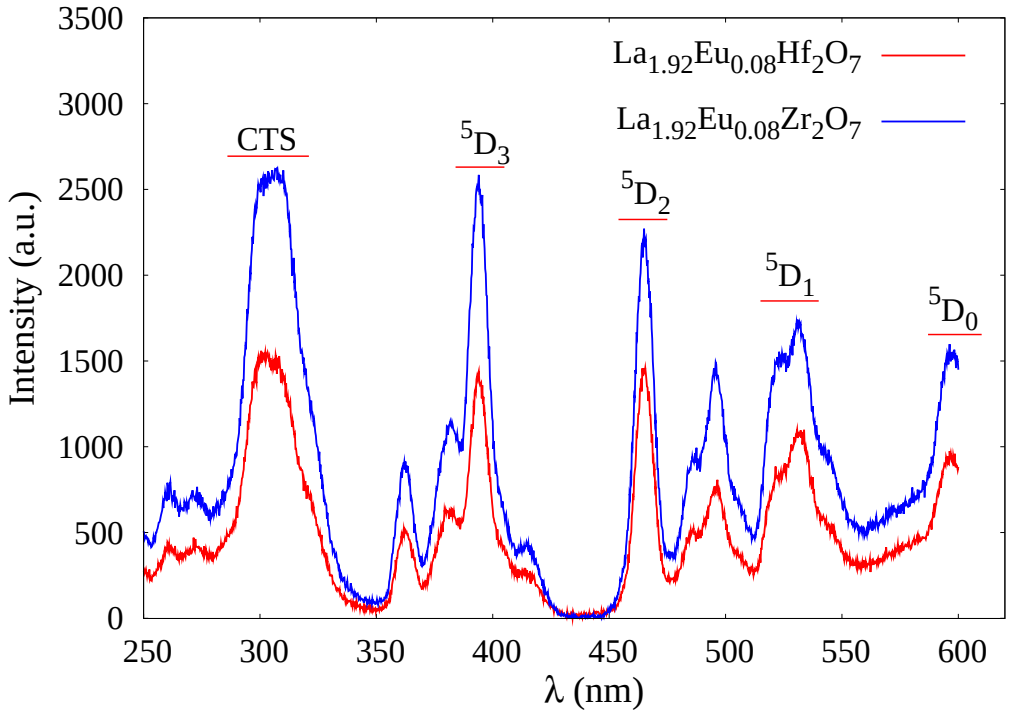

Figure 3.2 Excitation spectra for $La_{1.92}Eu_{0.08}Zr_2O_7$ and $La_{1.92}Eu_{0.08}Hf_2O_7$ for λ_{em}=611 nm. (6)

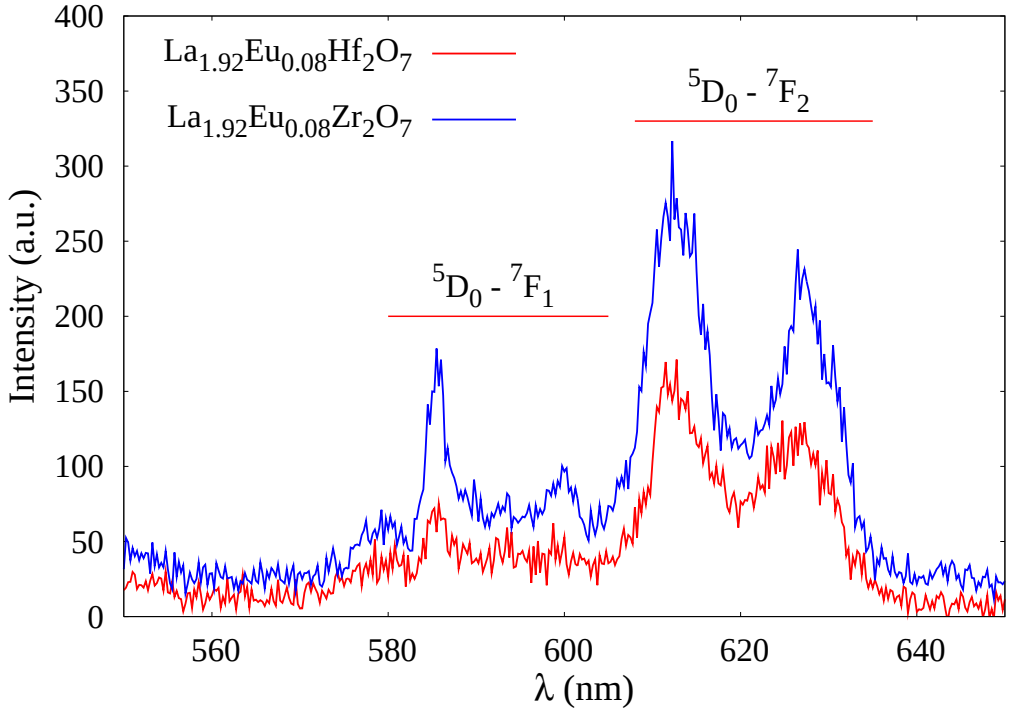

Figure 3.3 Emission spectra for $La_{1.92}Eu_{0.08}Zr_2O_7$ and $La_{1.92}Eu_{0.08}Hf_2O_7$ for λ_{exc}=337 nm. (6)

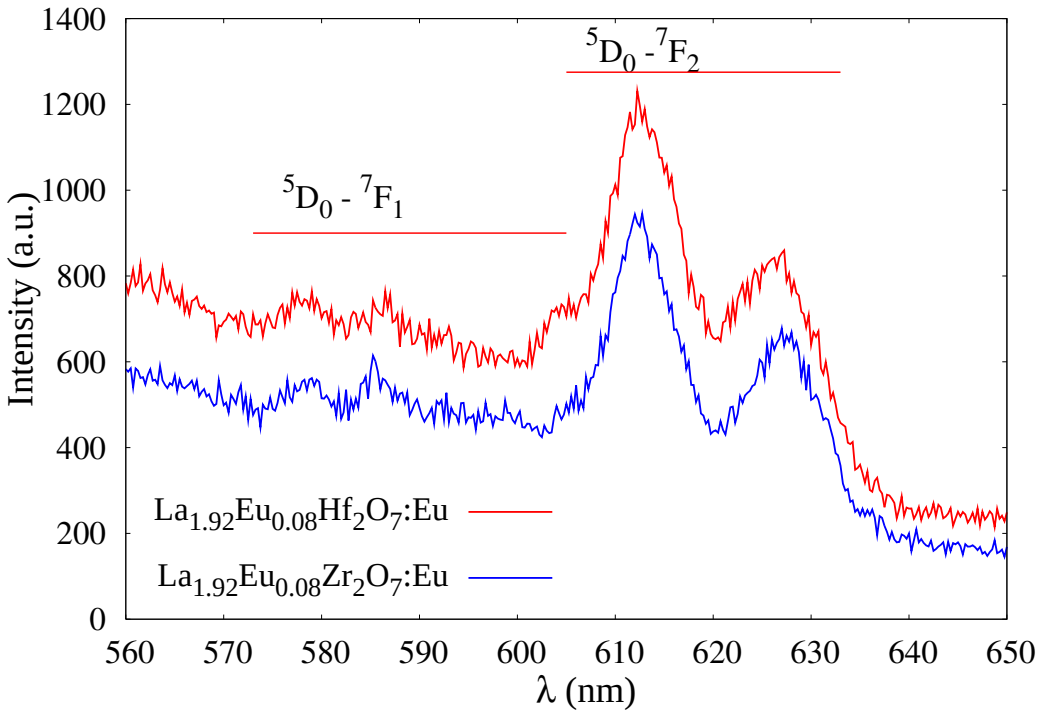

Figure 3.4 Emission spectra for $La_{1.92}Eu_{0.08}Zr_2O_7$ and $La_{1.92}Eu_{0.08}Hf_2O_7$ for λ_{exc}=532 nm.

report, but others have attributed multi-exponential decay to surface defects, concentration quenching effects, and multiple luminescent sites (29). The time constant was determined by measuring the logarithmic decay from 15% to 35% of the total luminescent signal after the excitation pulse was terminated. This portion of the signal captures the fast component of the decay curve. The error in the lifetime measurement was between 20-40 μs.

For $\lambda_{exc} = 337$ nm, the room temperature lifetime measurement of $La_{1.92}Eu_{0.08}Hf_2O_7$ is slightly less than that for $La_{1.92}Eu_{0.08}Zr_2O_7$. The luminescent lifetimes of both samples remained constant until ~673 K and then began decreasing exponentially to ~1073 K (Figure 3.6). The lifetime data for $La_{1.92}Eu_{0.08}Hf_2O_7$ seem to indicate that the luminescence may quench at slightly higher temperatures compared to $La_{1.92}Eu_{0.08}Zr_2O_7$.

A similar calibration curve is obtained with $\lambda_{exc} = 532$ nm for $La_{1.92}Eu_{0.08}Zr_2O_7$. The calibration curve with $\lambda_{exc} = 532$ nm for $La_{1.92}Eu_{0.08}Hf_2O_7$ is not shown because the

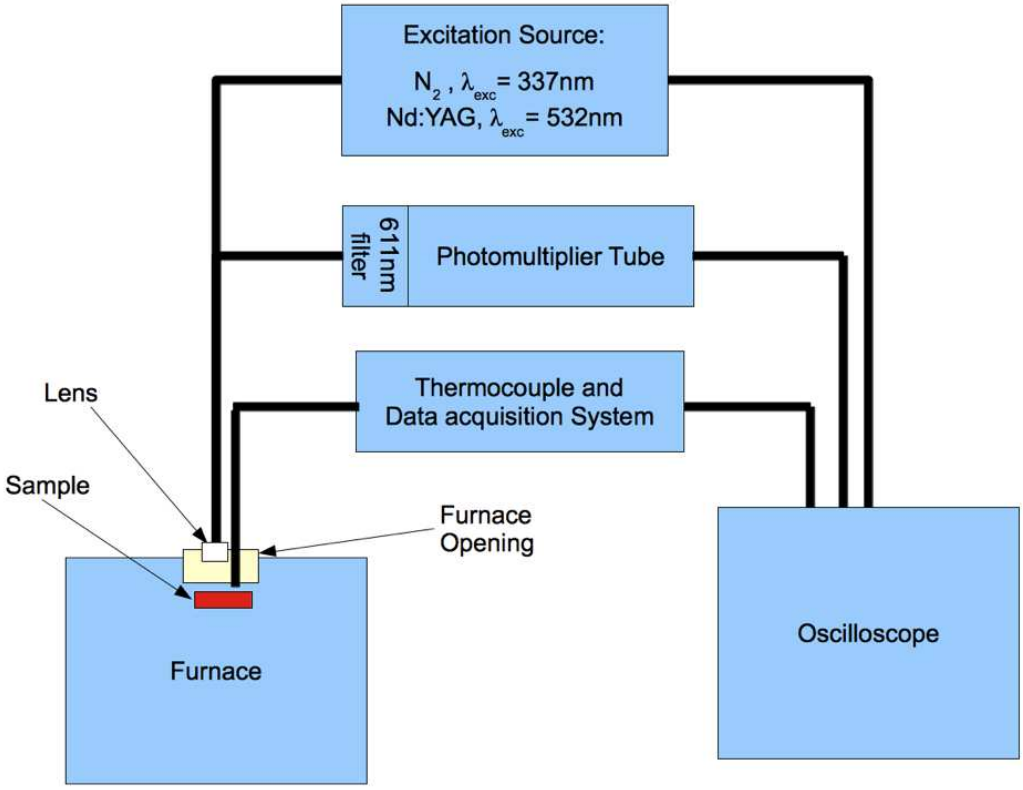

Figure 3.5 Experimental setup for temperature-dependent lifetime measurements

luminescent signal was indistinguishable from noise. The quenching temperature of each sample remained the same, regardless of the excitation wavelength, which will be examined by the configurational coordinate model in the following section.

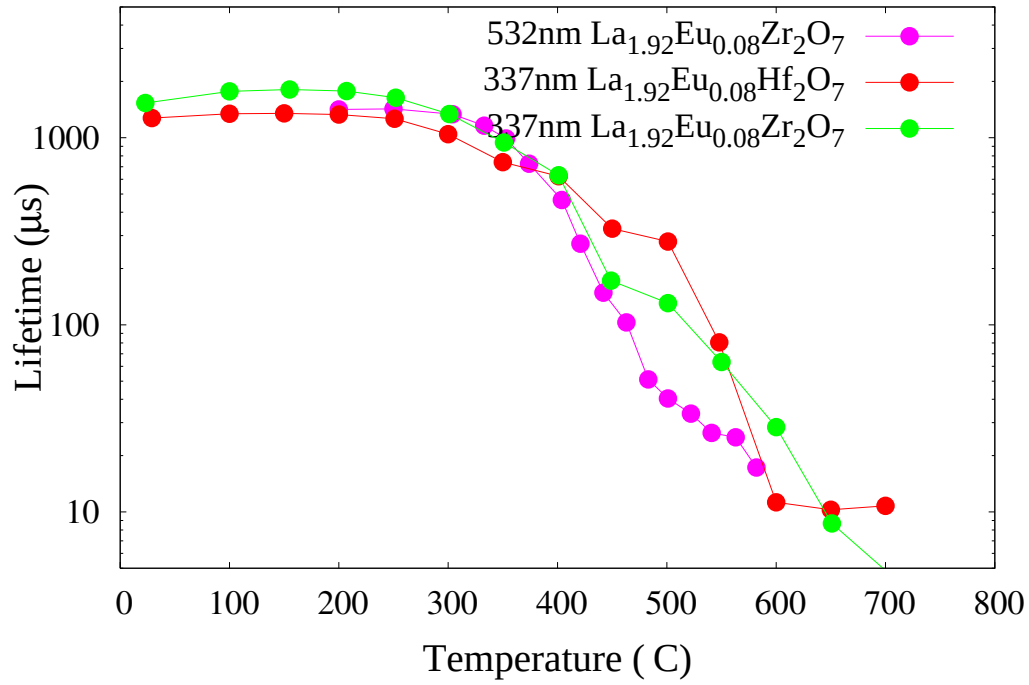

Figure 3.6 Lifetime measurements as a function of temperature for $La_{1.92}Eu_{0.08}Zr_2O_7$ and $La_{1.92}Eu_{0.08}Hf_2O_7$. λ_{exc}=337 nm, λ_{em}=611 nm.

Configurational Coordinate Model

A diagram of the configurational coordinate diagram for Eu^{3+} in pyrochlores is shown in Figure 2.2. The parabolic force constant, θ, is the same in both the excited and ground state. In the QMSCC model, θ represents the average phonon vibrational energy defined as $tan(\theta)^4 = \bar{h}\omega_v/\bar{h}\omega_u$, where $\bar{h}\omega_v = \bar{h}\omega_u = 400$ cm^{-1}.

The parabola offsets and relative energy differences were determined from the exci-

tation and emission spectra in Figure 3.2, 3.3, and 3.4. If $a_{uv} = 0$, the parabolas lie directly above each other and the band width of the optical transition vanishes which causes a single line to be observed. If $a_{uv} \neq 0$, the vibrational level of the lower state will have maximum overlap with multiple vibrational levels of the higher energy state and a broad excitation band is observed. Thus, the parabola offset increases with the width of the excitation peak. Figure 3.2 shows that the parabola offset between the $^5D_{0-3}$ states and the ground state is small because the excitation bands are relatively narrow and sharp. The excitation band for the charge transfer state is wider than the the other transitions, which indicates large parabola offset.

Excitation into the charge transfer state

For simplicity, the $^5D_0$, $^5D_1$, $^7F_2$, and the charge transfer state have been labeled as the t, u, g, and v states in Figure 2.2. The emission line of interest is the 611 nm line which corresponds to the $^5D_0 \rightarrow ^7F_2$ ground state. The quantum efficiency and lifetime of the$^5D_0 \rightarrow ^7F_2$ transition will be derived with the same approach described in Section II and follow the model used by (4).

The total rate at which energy quanta leave v, u, and t for g is

$$\sum = (u \rightarrow g)n_u + (v \rightarrow g)n_v + (t \rightarrow g)n_t \tag{3.1}$$

where n_u, n_v, and n_t are the populations for u, v, and t, respectively. The quantum efficiency of $(t \rightarrow g)$ is the ratio of emitted photons from t divided by all transitions to g:

$$\eta_{gt} = \frac{(t \rightarrow g)n_t}{\sum} = \frac{(t \rightarrow g)}{(u \rightarrow g)\frac{n_u}{n_t} + (v \rightarrow g)\frac{n_v}{n_t} + (t \rightarrow g)} \tag{3.2}$$

The the population ratios, $\frac{n_u}{n_t}$ and $\frac{n_v}{n_t}$, are found by the equations describing steady state

equilibrium:

$$G_v + (u \to v)n_u + (t \to v)n_t = (v \to u)n_v + (v \to t)n_v + (v \to g)n_v \tag{3.3}$$

$$G_u + (v \to u)n_v + (t \to u)n_t = (u \to v)n_u + (u \to t)n_u + (u \to g)n_u \tag{3.4}$$

$$G_t + (v \to t)n_v + (u \to t)n_u = (t \to v)n_t + (t \to u)n_t + (t \to g)n_t \tag{3.5}$$

where G_v, G_u, and G_t are the excitation rates into v, u, and t, respectively. Excitation into v, or the charge transfer state, means that $G_u = G_t = 0$. Consequently, Equations 3.4 and 3.5 can be used to define the population ratios:

$$\frac{n_u}{n_t} = \frac{(t \to u)}{(u \to t)} \left\{ \frac{(t \to v)(t \to g) - 1}{\frac{(u \to v)}{(v \to u)}(v \to t)(u \to g) + 1} \right\} \tag{3.6}$$

$$\frac{n_v}{n_t} = \frac{(u \to g, t, v)\frac{n_u}{n_t} - (t \to u)}{(v \to u)} \tag{3.7}$$

The quantum efficiency is found by substituting Equations 3.7 and 3.6 into Equation 3.2, and is rearranged as:

$$\eta_{gt} = \left\{ \frac{(u \to g)\frac{n_u}{n_t} + (v \to g)\frac{n_v}{n_t} + (t \to g)}{(t \to g)} \right\}^{-1} \tag{3.8}$$

The lifetime of the $t \to g$ transition is found by summing the populations in v, u, and t and by using Equation 3.2

$$\tau_t = \frac{(n_u + n_v + n_t)}{\sum} = \frac{(\frac{n_u}{n_t} + \frac{n_v}{n_t} + 1)}{(t \to g)}\eta_{gt} \tag{3.9}$$

Excitation into $^5D_1$ state

Excitation into the $^5D_0$ is accomplished by using the 532 nm excitation wavelength. Excitation into the u state in Figure 2.2 leads to non-radiative transitions from u to t via multiphonon emission and an upward, non-radiative transition from u to v and then another non-radiative transition from v to t. The possible radiative transitions from u are $u \rightarrow g$, $t \rightarrow g$, and $v \rightarrow g$. The total excitation rate is the same as in Equation 3.1 and the same quantum efficiency in Equation 3.2. However, excitation into u means that $G_v = G_t = 0$ and Equations 3.3 and 3.5 are used to find the population ratios.

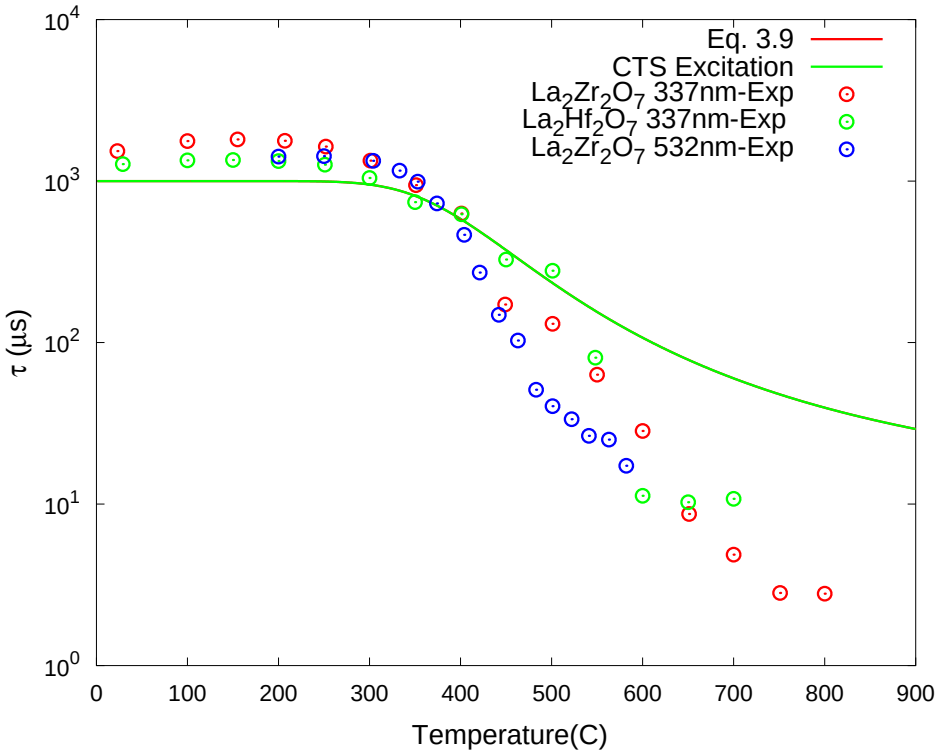

Figure 3.7 Equation 3.9 plotted along with lifetime measurements as a function of temperature for $La_{1.92}Eu_{0.08}Zr_2O_7$ and $La_{1.92}Eu_{0.08}Hf_2O_7$. λ_{exc}=337nm, λ_{em}=611nm.

Discussion

Figure 3.7 compares the experimental lifetime measurements with the calculated lifetimes using the configurational coordinate model. We have calculated the temperature-dependent lifetimes for excitation into two states: 1) the charge transfer states (337 nm excitation) and 2) the $^5D_1$ state (532 nm excitation). The emission line of interest is for the $^5D_0 \rightarrow ^7F_2$ transition ($t \rightarrow g$ parabola in Figure 2.2). However, Figure 3.7 shows that the temperature-dependence of the $^5D_0 \rightarrow ^7F_2$ lifetime is the same, regardless of the excitation source. The experimental data also show that the thermal quenching of 611 nm emission $La_{1.92}Eu_{0.08}Zr_2O_7$ is the same regardless of the excitation wavelength.

One possible explanation is that excitation into the CTS feeds rapidly into the lower ^5D states. The intersection of the *v* and *t* state is at the parabola minimum of *v*. Thus, at low temperatures, energy from the *v* state is most likely to be transfered to the *t* state. However, the *u* state is more likely to be populated as the temperature increases. Consequently, the population of the *t* state decreases, which decreases radiative transitions from *t* to *g*.

Excitation into the *u* state leads to a similar quenching temperature because the possible transition pathways remain the same. At low temperatures, excitation into *u* leads to a non-radiative transition from *u* to *t* and then a radiative transition from *t* to *g*. As the temperature increases, *u*-state excitation leads to an increase in the population of the *v* state. As the population of the *v* state increases, the population of the *t* state increases via non-radiative transitions from *v*, which leads to radiative emission from *t*. However, as the further temperature increases, non-radiative transitions from *v* to *u* is more likely. Consequently, this leads to a decrease in the population of the *t* state.

Although the excitation wavelength trend is the same in both experimental and calculated data, the exponential decrease of the experimental lifetime is significantly different than the calculated results. One reason for the discrepancy could be defects that allow for additional states not considered in the original model. The phosphors were made using combustion synthesis, which is known to produce highly-crystalline powders that

are composed of large single crystals and aggregated nanocrystals (7). The aggregated nanocrystals could provide additional surface states which could serve as traps for excitation. These additional states could serve as intermediate "bridges" for non-radiative energy transfer. These extra states could be represented as an additional state similar in energy as the charge-transfer state.

The quenching temperature is the same for both materials because the structures of $La_{1.92}Eu_{0.08}Zr_2O_7$ and $La_{1.92}Eu_{0.08}Hf_2O_7$ are very similar. The Eu^{3+} ion substitutes in the A site of the pyrochlore structure. The A site is located in a distorted cube (scalenohedra) and has a coordination number of 8. Six of the oxygens are at equal distance from Eu^{3+} and the other two oxygens are are at a slightly shorter distance from Eu^{3+} . Hirayama has shown that as the radii of the B decreases the distortion of the scalenohedra increases. The distortion of the scalenohedra increases magnetic dipole transitions and increase the splitting between the orange emission lines ($^5D_0 - ^7F_2$ transitions). (25) Thus, the ratio between the red and orange emission lines can be used to describe the symmetry of the Eu^{3+} environment. The red emission lines in Figure 3.3 and 3.4 show that the Eu^{3+} is in a low symmetry site since the electric dipole transitions dominate. However, Figure 3.3 shows that Eu^{3+} site in $La_{1.92}Eu_{0.08}Zr_2O_7$ is less distorted that Eu^{3+} in $La_{1.92}Eu_{0.08}Hf_2O_7$ because the orange emission lines are more intense than for the lanthanum hafnate. However, the difference in the emission spectra does not affect the lifetime measurements.

Although the relative ratio of emission between $La_{1.92}Eu_{0.08}Hf_2O_7$ and $La_{1.92}Eu_{0.08}Zr_2O_7$ is different, the peak wavelength is the same. Consequently, the relative energy differences between the electronic states is the same. Since the energetic locations of the electronic states don't change, the temperature-dependent lifetime does not change between the two materials.

Previously, Gentleman has shown that substituting certain elements on the A sites of pyrochloric compounds will produce materials that will emit at temperatures greater than 1000 °C (17). The quenching temperature of $Y_2Zr_2O_7$, $Sm_2Zr_2O_7$, Eu_2Zr_2O7, and

$Gd_2Zr_2O_7$ was highest for compounds where the atomic radius of the A elements was greatest: $Y_2Zr_2O_7$ and $Gd_2Zr_2O_7$. The larger elements on the A site stabilize the zirconia structure, which is related to the pyrochlore structure. In this study, we have substituted elements on the B site. B-site substitution with larger atoms has the effect of increasing the distortion of the Eu^{3+} environment which increases electronic dipole transitions. Likewise, the intensity of the red line emissions also increases. Also, the results of this experiment indicate that substitution on the B site does not have an effect on the quenching temperature.

The results of this work indicate that high quenching temperatures for Eu^{3+} ions in pyrochlore materials are obtained when the A site has atoms with larger atomic radii than atoms on the B site. The large atoms on the A site help to stabilize the pyrochlore structure. The stabilization of the lattice also results in higher energy for the charge transfer state, as seen from Figure 3 of reference (17). The peak absorption in the charge transfer state for $Sm_2Zr_2O_7$, Eu_2Zr_2O7, and $Gd_2Zr_2O_7$ was approximately 250nm, compared to 300nm for the materials in this study. The high energy of the charge transfer state acts as a "bridge" which carries energy from thermally populated states of $^5D_1$ back to $^5D_0$. Luminescence begins to quench at low temperatures because the energy difference between the parabola minimum of the charge transfer state and the $^5D_1$ state is smaller in $La_{1.92}Eu_{0.08}Hf_2O_7$ and $La_{1.92}Eu_{0.08}Zr_2O_7$. Conversely, it has been shown that materials with high quenching temperatures also have high energy charge transfer states. For example, the charge transfer state in YAG:Eu is approximately 275nm and the thermal quenching of the $^5D_0 \rightarrow 4f$ does not begin until $\approx 800\ ^\circ$C (30), (31). Furthermore, the quenching temperature of $YBO_3 : Eu$ is $\approx 700\ ^\circ$C , which has a charge transfer state absorption at 254nm (31), (32).

Chapter Summary

The data from this work and others indicate that Eu-doped materials with high-energy charge transfer state exhibit higher quenching temperatures. Excitation into the charge transfer states directly feeds into the $^5D_1$. High temperature causes the vibrational

levels of the $^5D_1$ to be thermally populated which leads to crossover to the $^5D_0$ state. The quenching temperature of $La_{1.92}Eu_{0.08}Zr_2O_7$ and $La_{1.92}Eu_{0.08}Hf_2O_7$ were lower than materials tested by Gentleman, most likely because of the lower charge transfer state.

The configurational coordinate model for $La_{1.92}Eu_{0.08}Zr_2O_7$ and $La_{1.92}Eu_{0.08}Hf_2O_7$ was used to calculate the temperature-dependent lifetime for the $^5D_0 \rightarrow 4f$ transition. Although this model correctly predicted the quenching temperature, this model did not accurately represent the experimental lifetime data at higher temperatures. This is most likely because the model does not take into account the influence of defects within the pyrochlore structure. The pyrochlore structure is very similar to the YSZ, which is known to be riddled with oxygen vacancies, which act as traps for luminescence (33).

CHAPTER IV

YTTRIUM ALUMINUM GARNET

Introduction

Cerium-doped yttrium aluminum garnet ($Y_3Al_5O_{12}$:Ce, YAG:Ce) is a prime candidate for use as a thermographic phosphor because it is chemically inert, able to withstand corrosive environments, and has an intense broad-band yellow-green emission. There are multiple excitation bands in the uv and visible regions. The emission is temperature-dependent over the range 77-300°C and the decay time is $\sim$ 60ns (34).

The cubic structure of yttrium aluminum garnet is highly symmetric and has the formula $A_3B_5O_{12}$. The lattice parameters can be tuned by substitution on either the A or B site of the YAG structure. The Ce^{3+} atoms substitute for Y^{3+} and are located in a dodecahedral site that is coordinated with 8 oxygens. Atoms in the B site are in tetrahedral or octahedral oxygen cages. Substituting atoms on the B site with radii larger than Al^{3+} compresses the oxygen cage surrounding the A-site atom. This compression on the dodecahedral results in a blue-shift of the emission wavelength (35).

The photoluminescence of cerium-doped phosphors has been extensively studied because of the unusual interactions between the excited states and the host lattice. Typically, rare-earth ions emit from the well-shielded 4f orbitals and therefore are not significantly affected by the host lattice. However, Ce^{3+} is different because there is only one electron in the first shell of the 4f orbital ($4f^1$ electron configuration). Consequently, electrons are excited to and emit from the high-energy 5d orbitals. The relative energy of the 5d orbitals is highly dependent on the host lattice. Substitution of atoms in the B site for larger atoms, such as Ga^{3+} , results in a decrease in d-orbital splitting. The reduction in splitting results in a blue shift in the emission wavelength. (35) The emission peak also

becomes broader as gallium is substituted into the YAG lattice.

The reduction in splitting of the d-orbitals also affects the emission lifetime, especially at higher temperatures. The luminescent lifetime of bulk YAG:Ce at room temperature is approximately 60ns and will remain constant until about 150 °C (this temperature will be referred to as the quenching temperature). After 150 °C the lifetime decreases to $\sim$10 ns at 300 °C . In this experimental study, Al^{3+} ions for Ga^{3+} (YAGG:Ce) were substituted in order to determine the effect on the calibration curve. (36) showed that substituting Ga^{3+} ions in place of Al^{3+} ions shifts the emission to shorter wavelengths and a red-shift in the excitation spectra. The excitation and emission properties of YAGG:Ce have been extensively studied and are well documented. However, little has been reported about the temperature-dependence of gallium-substituted YAG:Ce.

Synthesis

We have synthesized a series of garnet phosphors with the formula $Y_{2.97}(Al_{1-x}Ga_x)_5O_{12} : Ce_{0.03}$ (where x=0, 0.25, 0.50, 0.75, 1.0) via a simple combustion synthesis method. In a combustion synthesis reaction, rare-earth nitrates and an organic fuel (urea) are dissolved in a small amount of water and placed in a muffle furnace at 500 °C for about 10 minutes. During this time the water is boiled off and the nitrates and fuel reach their ignition temperature which drives the formation of the phosphor. The reaction produces highly crystalline, luminescent powder and produces approximately 10 grams of product for this experiment. All samples were calcined in air at 1000 °C for 5 hours to remove any impurities.

Morphology

Although combustion synthesis is a simple and rapid technique, the morphology of the products are not uniform. Figures 4.2 and 4.1 show that combustion synthesis produces

micron-sized single crystals and aggregated nanocrystals. Nanocrystalline phosphors have been shown to behave differently from bulk materials due to the large number of surface defects relative to the volume of the crystal (37). However, we have used X-ray diffraction to compare our samples to commercially available bulk and nanocrystalline YAG:Ce (Figure IV). Our sample does show some line broadening which is the result of small crystalline size or non-uniform distortions. However, the peak 2θ values for our sample and bulk sample are nearly identical indicating that the nanocrystalline component of our samples is minimal.

X-Ray Diffraction

The effects of gallium substitution are readily observed using X-ray diffraction (XRD) and are shown in Figure 4.4. The peak shift to the left indicates that the interplanar spacing increases with the molar amount of gallium. Likewise, the lattice constant also increases from 12.0 Å to approximately 12.2 Å as the gallium content increases from 0-75%. The structural changes in the tetrahedral and octahedral cages result in a decompression of the cubic-like oxygen cage that surrounds the Ce^{3+} ions. This decompression around the Ce^{3+} ion changes the energetic location of the lowest 5d orbitals, which effects the excitation and emission properties.

Photoluminescence

Upon excitation via a UV light source, electrons are excited to the d_2 excited state of the 5d levels. The splitting of the d_2 and d_1 states in the 5d levels is directly related to the bonds from the cerium ion to the surrounding oxygen atoms. The cerium ion in the garnet structure is surrounded by eight oxygens which form a cube-like structure. In YAG unit cells, the “cube” is highly compressed into a tetragonal distortion (See Figure 4.5). This distortion increases the splitting between the d_2 and d_1 excited states. Emission occurs from

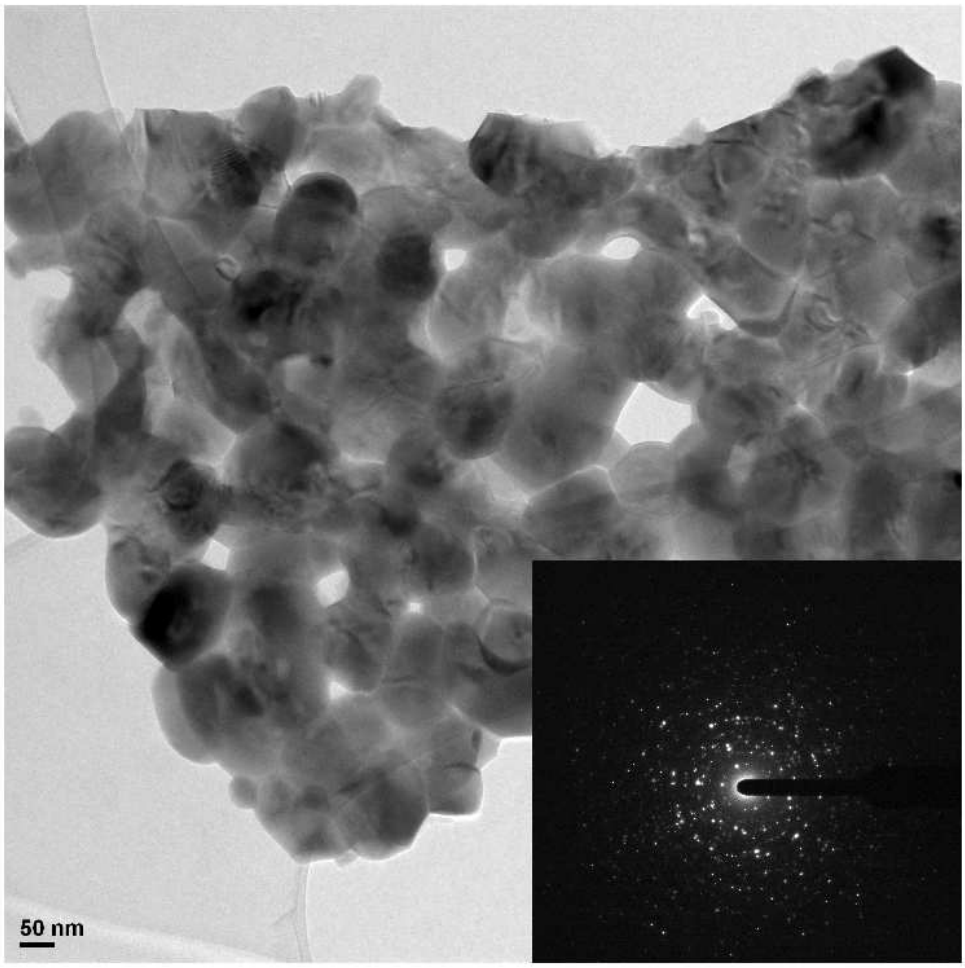

Figure 4.1 Bright-field image of well-defined YAG:Ce nano-crystallites and diffraction pattern. (7)

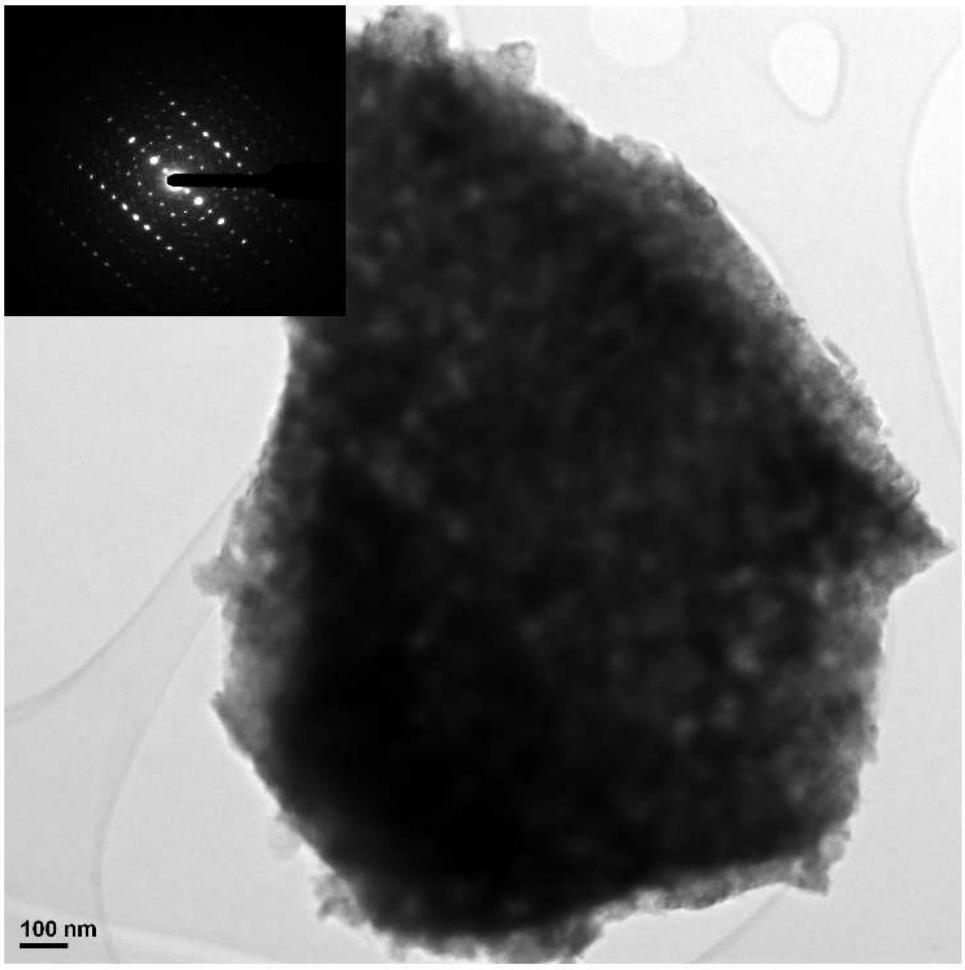

Figure 4.2 Bright-field image of large single YAG:Ce crystal and diffraction pattern. (7)

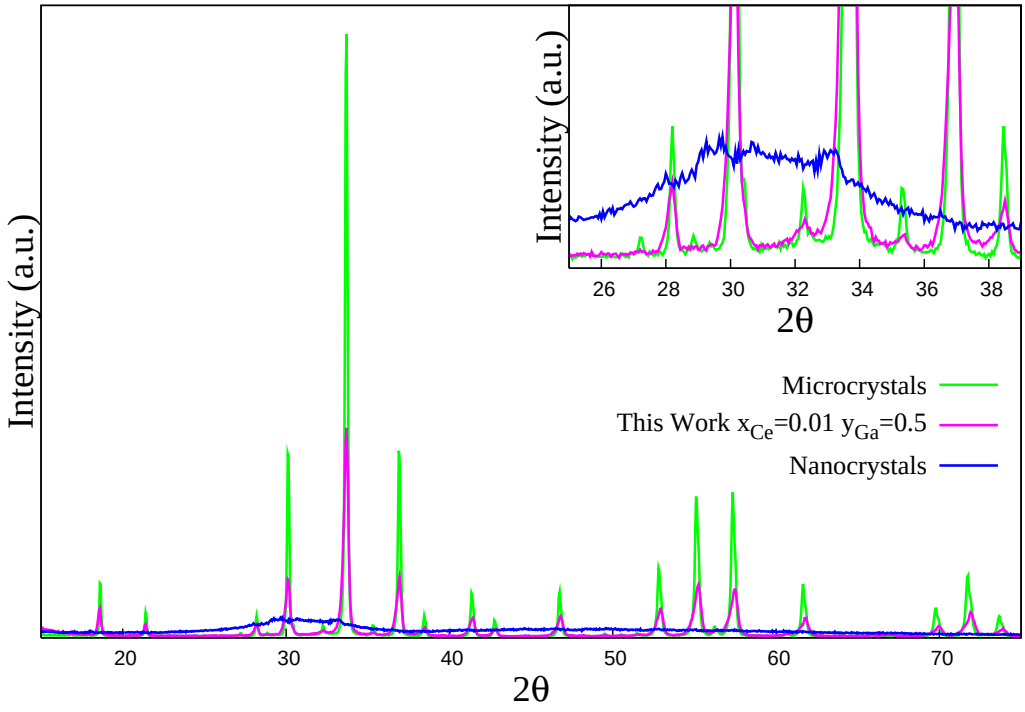

Figure 4.3 Comparison of diffraction patterns of combustion-synthesized YAG:Ce with commercially available microcrystals and nanocrystals. (7)

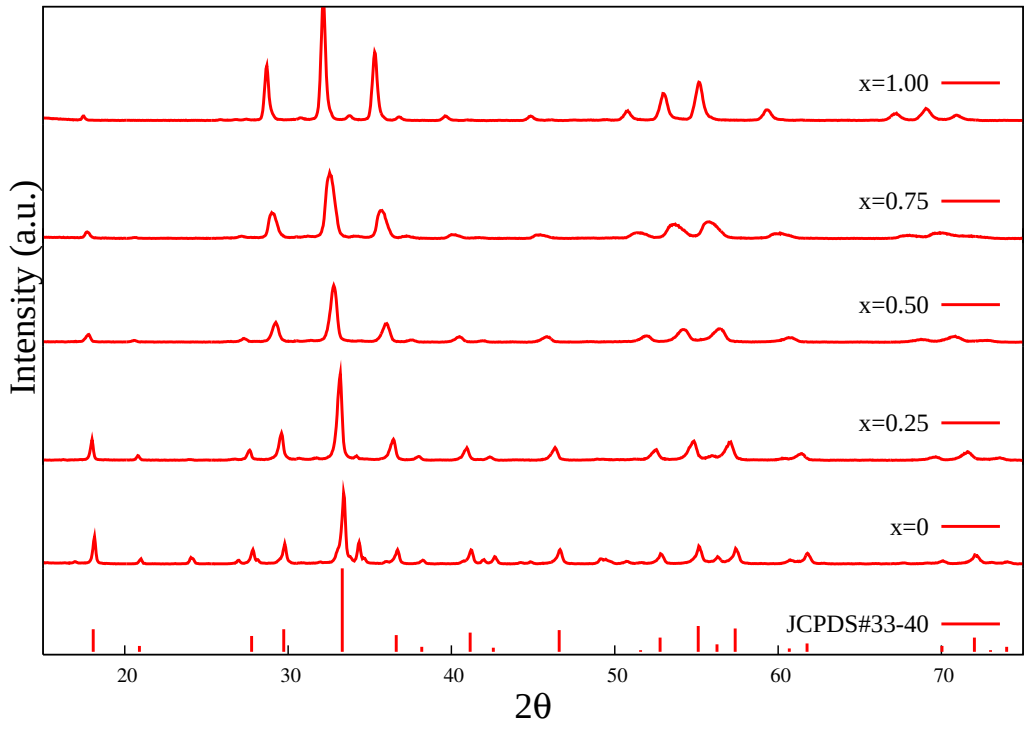

Figure 4.4 X-ray diffraction patterns for $Y_{2.97}(Al_{1-x}Ga_x)_5O_{12} : Ce_{0.03}$. (7)

the lowest crystal field component of the 5d configuration. Since the splitting increases, the lowest component of the 5d configuration is now closer in energy to the ground state configuration. The result is the that cerium-doped YAG crystals have long emission wavelengths. In contrast, the luminescent ion in YGG is still in the A site, but the surrounding oxygens are more cubic in structure. This decompression of the cubic structure results in a smaller splitting of the d_2 and d_1 states of the 5d levels. Likewise, the energy gap between the lowest excited state and ground states is much higher compared to YAG. Thus, increasing gallium content in YAG decreases the emission wavelength. Sample emission spectra of YAG and YGG are shown in Figure 4.6.

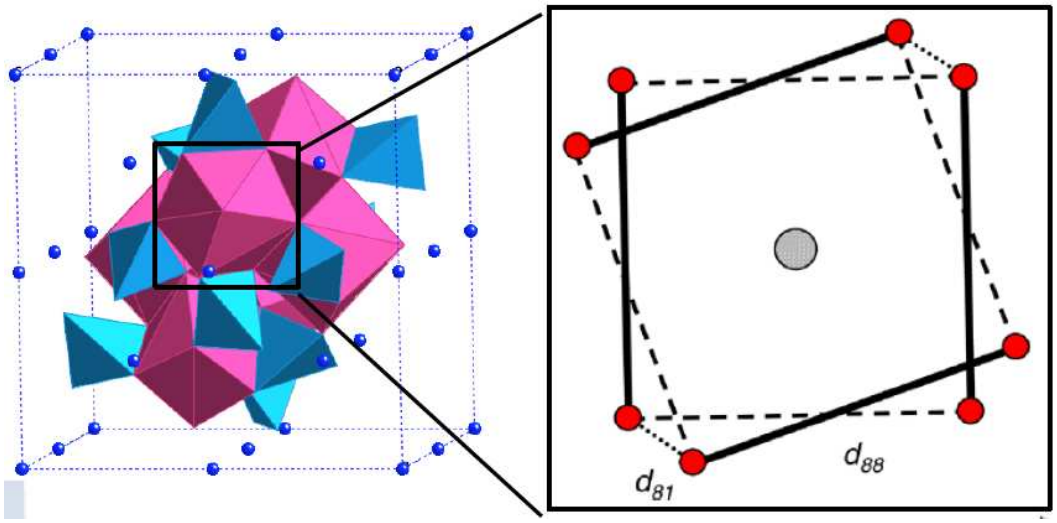

Figure 4.5 Garnet unit cell shown in polygon form. Each vertex is an oxygen atom. The blue tetrhedrons have aluminum (or gallium) ions in the central location and the purple dodecahedron have yttrium (or cerium) at the central location. The image on the right shows the environment of the cerium atom. In YAG, the ”cube” is tetragonally distorted, whereas in YGG, the cerium ion is in a more cubic environment.

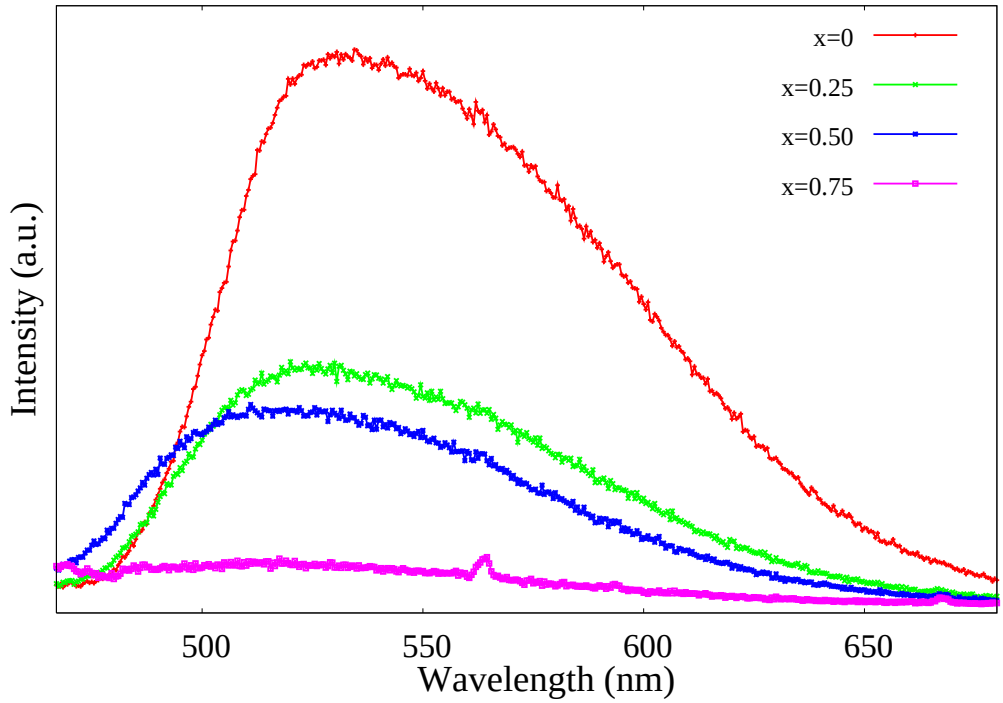

Figure 4.6 Emission spectra for $Y_{2.97}(Al_{1-x}Ga_x)_5O_{12} : Ce_{0.03}$ for λ_{exc}=460 nm. (7)

Temperature-Dependent Lifetime

The temperature dependence was determined using the configuration shown in Figure 4.7. The excitation source was a nitrogen laser (Laser Science Corporation, model VSL-337ND) with λ_{exc}=337 nm and an excitation band width of 0.1nm. The pulse width was 4 ns at a characteristic energy of 300 μJ. The excitation pulse was conveyed via an optical fiber to a 50:50 2×1 fiber optic splitter. The side of the splitter with the single fiber delivers the light to the sample. This same fiber collected and transmitted the emitted signal back through the splitter to a photomultiplier tube which served as the detector. Each phosphor sample was placed in the bottom of the plastic capsule which covered the excitation and detector fiber. The capsule/fiber was placed in an oil bath and slowly heated at a rate of 1 °C /min. A k-type bare wire thermocouple (Omega Engineering 871), which was placed near the capsule, monitored the temperature of the phosphor. Bandpass filters centered at 540 nm and 700 nm were used to collect the emitted signal. A waveform processing oscilloscope with 350 Hz bandwidth displayed, digitized, and stored the data.

Figure 4.8 shows the room-temperature decay time with respect to the amount of gallium and the decay lifetime as a function of temperature. The main observations from these data are 1) increasing gallium content decreases the luminescent lifetime and 2) high concentrations (>50%) of gallium lower the temperature range over which the lifetime is temperature-dependent. The error for the lifetime is $\pm$ 1-5 ns. (38) has shown that the error in the lifetime measurement can correspond to an error in temperature of 0.05 - 0.15 °C .

Configurational Coordinate Model

Sample configurational coordinate diagrams for the Ce-doped garnet system is shown in Figure 4.9.

The phonon energies are defined as $tan(\theta)^4 = \bar{h}\omega_v/\bar{h}\omega_u$, where $\bar{h}\omega_v = \bar{h}\omega_u = 400$

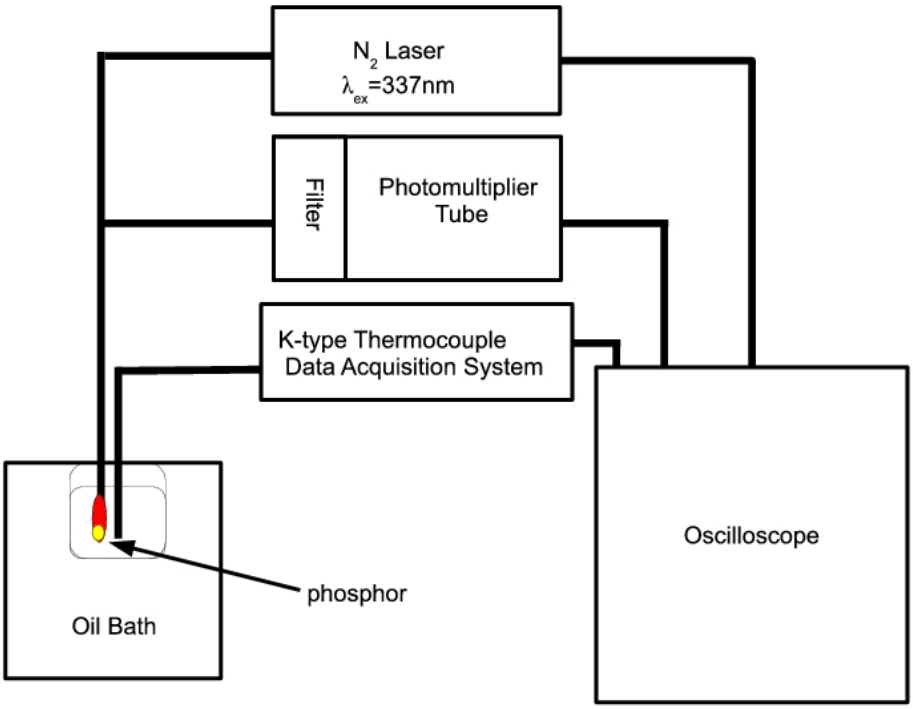

Figure 4.7 Fluorescent Temperature-Dependent Experimental Setup

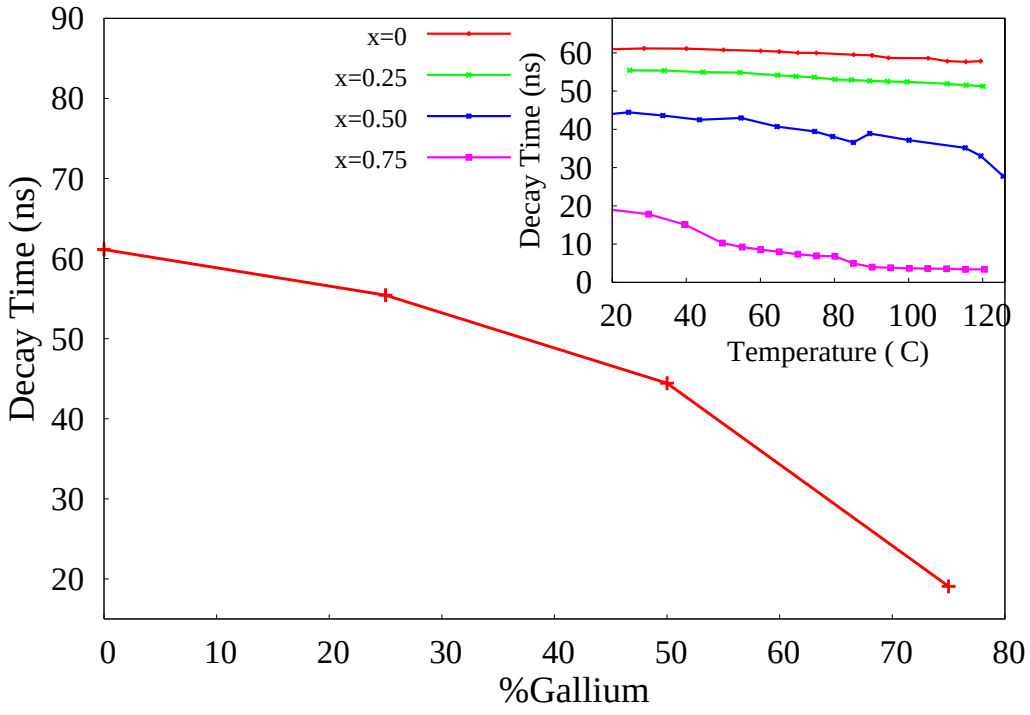

Figure 4.8 Luminescent lifetime (at 20 °C) as a function of gallium concentration and as a function of temperature (inset). λ_{exc}=337 nm, λ_{em}=540 nm. Reference: [(8)]

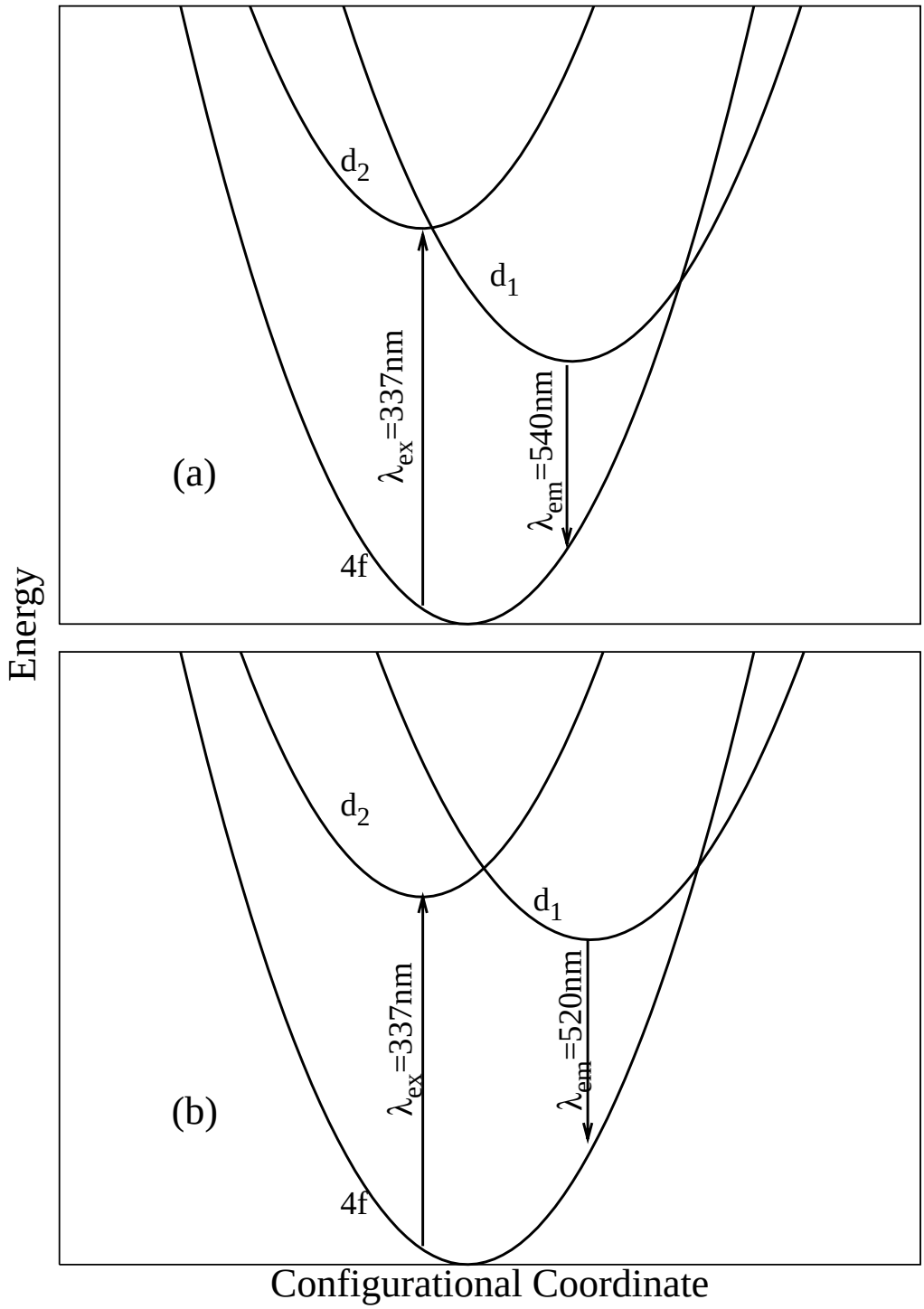

Figure 4.9 Configurational coordinate diagram that for (a)YAG and (b)YAGG

cm^{-1}, after (4). The parabola offsets and energy differences were determined from spectral data. The emission line of interest is the 540 nm peak emission caused by the $d_1 \rightarrow 4f$ transition. The excitation wavelength in the experiment was 337 nm which directly excites the d_2 state.

The total rate at which excitation leaves d_2 and d_1 for the $4f$ is:

$$\sum = (d_2 \rightarrow 4f)n_{d_2} + (d_1 \rightarrow 4f)n_{d_1} \tag{4.1}$$

where n_{d_1} and n_{d_2} are the populations for d_1 and d_2, respectively. The quantum efficiency for the $d_1 \rightarrow 4f$ transition is

$$\eta_{4f,d_1} = \frac{(d_1 \rightarrow 4f)n_{d_1}}{\sum} = \frac{(d_1 \rightarrow 4f)}{(d_2 \rightarrow 4f)\frac{n_{d_2}}{n_{d_1}} + (d_1 \rightarrow 4f)} = \left\{ \frac{(d_2 \rightarrow 4f)}{(d_1 \rightarrow 4f)} \frac{n_{d_2}}{n_{d_1}} + 1 \right\}^{-1} \tag{4.2}$$

The population ratio, $\frac{n_{d_2}}{n_{d_1}}$, is found using the steady state equilibrium equations

$$G_{d_2} + (d_1 \rightarrow d_2)n_{d_1} = (d_2 \rightarrow d_1)n_{d_2} + (d_2 \rightarrow 4f)n_{d_2} \tag{4.3}$$

$$G_{d_1} + (d_2 \rightarrow d_1)n_{d_2} = (d_1 \rightarrow d_2)n_{d_1} + (d_1 \rightarrow 4f)n_{d_1} \tag{4.4}$$

The Ce-doped garnets were excited with a 337 nm excitation source which excites the higher energy state, d_2. Therefore, $G_{d_1} = 0$ and the population ratio, $\frac{n_{d_2}}{n_{d_1}}$, is

$$\left. \frac{n_{d_2}}{n_{d_1}} \right|_{G_{d_2}} = \frac{(d_1 \rightarrow d_2, 4f)}{(d_2 \rightarrow d_1)} \tag{4.5}$$

The quantum efficiency for $d_2 \rightarrow 4f$ transition with d_2 excitation is found by substituting Equation 4.5 into Equation 4.2

$$\left. \eta_{4f,d_1} \right|_{G_{d_2}} = \left\{ \frac{(d_1 \rightarrow d_2)(d_2 \rightarrow 4f)}{(d_2 \rightarrow d_1)} + 1 \right\}^{-1} \tag{4.6}$$

The lifetime, τ_{d_1}, of the d_1 state with d_2 excitation is found by using Equation 4.2

$$\tau_{d_1}\Big|_{G_{d_2}} = \frac{n_{d_1}+n_{d_2}}{\sum} = \frac{n_{d_1}+n_{d_2}}{(d_1 \rightarrow 4f)n_{d_1}} \left(\eta_{4f,d_1}\Big|_{G_{d_2}} \right) \tag{4.7}$$

The inverse rates $(d_2 \rightarrow d_1)$ and $(d_1 \rightarrow d_2)$ are related by $(d_2 \rightarrow d_1)/(d_1 \rightarrow d_2) = r_0^{pU}$ because of the summed thermal weight definition in Equation 2.16 and the symmetric relationship $< u_x|v_y >^2 = < u_y|v_x >^2$ for overlap integrals with $\theta = 45^\circ$. Using the inverse relationship, the lifetime can be simplified to

$$\tau_{d_1}\Big|_{G_{d_2}} = \frac{1 + r_0^{pU,(d_2 \rightarrow d_1)} + \frac{(d_1 \rightarrow d_2)}{(d_1 \rightarrow 4f)}}{(d_1 \rightarrow d_2)(d_2 \rightarrow 4f) + (d_2 \rightarrow d_1)} \tag{4.8}$$

The radiative transitions are $(d_1 \rightarrow 4f)$ and $(d_2 \rightarrow 4f)$ which have the rate $R_{4f,d_1} = 10^3\ s^{-1}$. The non-radiative transitions are $(d_1 \rightarrow d_2)$ and $(d_2 \rightarrow d_1)$ and have the rates $N_{d_1,d_2} Up_{d_1}$ and $N_{d_2,d_1} Up_{d_2}$, respectively. The summed thermal weights, Up_{d_1} and Up_{d_2} , are defined in equation 2.16. Equation 4.8 is plotted along with experimental data in Figure 4.10.

Discussion

Figure 4.9 (a) shows the configurational coordinate diagram for Ce^{3+} in YAG. Electrons are excited to the d_2 state of the 5d orbitals using an excitation wavelength of 337 nm. Energy is then transfered non-radiatively from the lowest vibrational level of the d_2 state to high vibrational levels of the d_1 state. Radiative emission occurs from the lowest vibrational level of the d_1 state to the 4f ground state. At high temperatures, electrons can be promoted from the lowest vibrational levels of the d_1 state back up to the crossover point of the d_1 and 4f parabola. Consequently, energy will be transfered non-radiatively to the ground state. As a result, the observed lifetime will decrease as a function of increasing temperature.

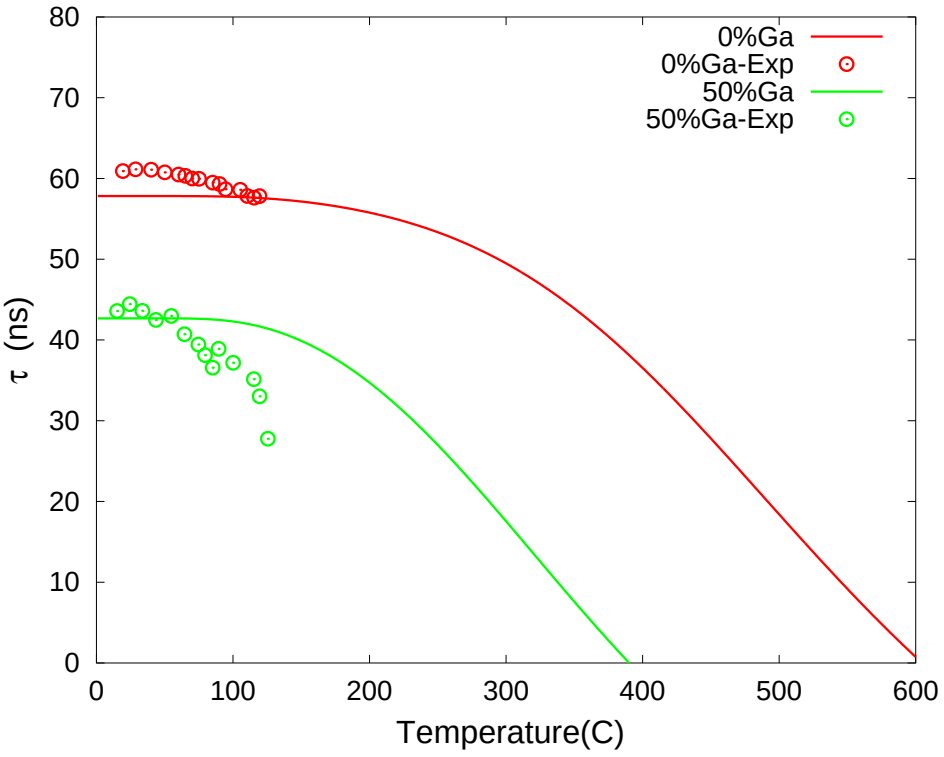

Figure 4.10 Experimental and calculated thermal quenching of $d_1 \rightarrow 4f$ emission for 0% and 50% gallium substition

The energy transfer process is the same in YAGG (Figure 4.9 (b)). Excitation of the phosphor using 337 nm wavelength will promote electrons to the d_2 state and then energy will be transfered to the d_1 state. Emission will occur from the lowest vibrational level of the d_1 state. However, the splitting between the d_2 and d_1 is much less in YAGG compared to YAG which means that less energy required to promote electrons up to the crossover point, Δ_{YAGG}. Therefore, luminescence quenching occurs at lower temperatures in gallium substituted garnets as compared to YAG.

Figure 4.10 compares the experimental data with the calculated temperature-dependent lifetime in equation 4.8. The temperature range of the current data is not wide enough to accurately compare with the configurational coordinate model. However, the general trend is commensurate with experimental data. For example, the low-temperature lifetime of the 0% Ga-substituted sample is longer than the lifetime for the 50% Ga-substituted sample which corroborates with the data shown in Figure 4.8. The reason for the decrease in lifetime as the percentage of Ga increases is because of the decrease in splitting of the the lowest *d* orbitals.

According to Equation 4.8, the quenching temperature decreases as the percentage of gallium substitution increases. The experimental data for the 50% Ga-substitution sample also shows a lower quenching temperature for higher amounts of gallium. This can be explained by referring to the configurational coordinate diagrams in Figure 4.9. We are interested in the temperature-dependence of the $d_1 \rightarrow 4f$ transition. Samples with no gallium substitution have a large splitting between the lower *d* orbitals. At low temperatures, excitation into d_2 feeds non-radiatively into d_1. A radiative transition from d_1 to the $4f$ state follows. As the temperature rises, excitation energy fed into d_1 from d_2 is now available to thermally populate d_1 levels. The transition from d_1 to $4f$ at the parabola crossover is now likely because the lower vibrational levels of d_1 are now thermally populated.

When gallium is substituted into the YAG structure, the splitting between the *d* orbitals decreases. The decrease in splitting results in a lowered energy required to crossover

to high vibrational levels of the $4f$ state at the parabola crossover. Equation 4.8 shows that the quenching temperature for 0% gallium substitution is approximately 150 °C , which agrees well with previous results (34). However, the CCD model overestimates the low temperature lifetime by a factor of 2. One reason for this discrepancy could be because of the estimation in the R_{uv}, which is the from the electronic portion of the integral. The CCD model of Struck and Fonger does not consider the variation in thermal quenching calculations.

Trivalent cerium in YAG is unique among the rare earth elements because the major luminescent transition occurs from the interaction between the high-energy, 5d-orbitals, whereas the other lanthanoids exhibit luminescent transitions originating from the 4f orbitals. Since the 5d-orbitals are not as shielded from the influence of the lattice, visible luminescence of Ce^{3+} is significantly affected by the surrounding lattice. The splitting of the 5d-orbitals affects the temperature-dependent emission properties. The lower $5d_1$ orbital acts as a "bridge" to carry energy non-radiatively to high vibrational levels of the 4f states. The smaller the splitting between the two states means that lower energies are needed to crossover to the ground state. Therefore, higher quenching temperatures are obtained by substituting atoms into the B site with atomic radii smaller than atoms in the B site.

Kottaisamy and others have shown that partially substituting atoms such as Gd^{3+} or La^{3+} in the A site increases the emission wavelength of the Ce^{3+} atom (39). Substitution on the A site with atoms of the same atomic radii or greater of Y^{3+} has the effect of increasing the splitting between the 5d-orbitals. Therefore, it is likely that these materials may prove to exhibit higher quenching temperatures with partial A-site substitution.

CHAPTER V

SUMMARY

Configurational Coordinate Model

The QMSCC models used to predict thermal quenching of luminescent materials is an effective tool for the evaluation of phosphor materials for use as thermographic phosphors. Previous work has shown that this model works well for predicting the quenching temperature of several other phosphor materials, such as YAG:Cr^{3+} , $Al_2O_3 : Ti^{3+}$, and $LiSrAlF_6 : Cr^{3+}$ (4) (40) (23). The model assumes that only one vibrational mode is dominate and therefore can be described by a single configurational coordinate. This interaction coordinate describes the motion of two bonded atoms, which, for this work, was the motion between the rare-earth ion and the neighboring oxygen atom. This simplification of vibrational motion greatly reduces the computational complexity of the problem. Both ground and excited states are assumed to be harmonic and therefore exhibit a parabolic relationship between energy and the configurational coordinate. The energy of the excited states is determined from the peak wavelength of the excitation bands. The configurational coordinate, or the parabola offset, of the excited states is determined geometrically from the width of the excitation band. In general, broad band excitations indicate large parabola offset, where as narrow line excitation bands indicate small parabola offset. The ability to determine the location of energy states from readily-available spectral data is advantageous, compared to calculating energy states from first principles. Transitions between states are calculated using Manneback's recursion formulas, which exactly determine the Condon overlap integral (20). The input parameters needed to determine the overlap integrals are obtained from spectral data. The temperature-dependence of the luminescence is determined by using the summed thermal weights described in equation 2.16. The total non-radiative rate between

two states is determined by summing over all resonant vibrational initial and final states for a particular energy transition and then multiplying by a non-radiative frequency factor, N_{uv}. The total radiative rate is summed over all initial and final states for a given energy. However, the thermal weights form a normalized distribution summing to unity such that the total radiative is approximately R_{uv}.

In order to determine the lifetime of a particular transition, it is nessecary to determine the population of the excited states. By knowing which state was excited in the experiment, the steady state equations for the excited states are used to calculate excited state populations (in ratios). Although this model is semi-empirical, the QMSCC accurately predicts trends within phosphor materials, as shown in Figure 4.10. In this work, we have shown that the QMSCC accurately predicts the quenching temperature for Ce-doped YAG and for Eu-doped pyrochlores.

Unfortunately, the QMSCC model does not always accurately predict thermal quenching after thermal quenching begins (i.e. at temperatures higher than the quenching temperature), as shown in Figure 4.10. One reason for the discrepancy could be because the frequency factor for radiative and non-radiative transitions, N_{uv} and R_{uv} is considered constant. These constants are taken from the electronic portion of the transition integral and have been shown to vary over several orders of magnitude (41). Improvements in predicting thermal quenching may result from the variation or exact calculation of the frequency factor for both radiative and non-radiative transitions. Additional improvements could come from variation of $\bar{h}\omega$ in both the initial and final states. In this work, we have assumed that $\bar{h}\omega_u = \bar{h}\omega_v$. Physically, equal force constants means that the force between atoms is exactly the same in the ground state as in the excited state. In fact, theoretical studies have shown that variation of the force constants in initial and final states does not improve the ability of the model to predict thermal quenching (23). However, excitation into high energy states, such as charge transfer states or d-orbitals for Ce^{3+} , greatly alters the equilibrium bond distance (increases the parabola offset) and it is unlikely that the force constants are equal

for these high energy states.

Thermographic Phosphors

Comparison of the experimental results with the calculated results of the QMSCC model reveal important relationships between 4f energy states of the rare-earth elements and energy states that are highly influenced by the lattice. Using rare-earths for thermographic phosphors is highly advantageous because the 4f-orbitals of the lanthaniods are highly shielded from the surrounding environment. As a result, the energies of the 4f $\rightarrow$ 4f transitions remain relatively constant, regardless of the lattice. However, the intense yellow-green emission from Ce^{3+} is the result of a transition from the high-energy *d*-orbitals. Unlike the 4f-orbitals, the *d*-orbitals are highly influenced by the surrounding lattice. Furthermore, the splitting of the two lowest *d*-orbitals greatly influences the thermal quenching of the $d_1 \rightarrow 4f$ transition. We have shown that the splitting of the two lowest *d*-orbitals decreases as gallium is substituted into the YAG lattice. The decrease in splitting reduces the quenching temperature.

The intense narrow-line, red emission from Eu^{3+} is the result of a 4f-4f transition: $^5D_0 \rightarrow 4f$. However, the rate at which the $^5D_0$ is filled greatly influences the thermal quenching. The $^5D_0$ is fed from the charge transfer state, which is highly influenced by the lattice. The quenching temperature of the Eu-doped pyrochlores in this work was approximately 300 °C and did not exhibit any visible emission after 600 °C . The quenching temperature of other Eu-doped pyrochlores has been as high as 800 °C and visible emission was observed until well above 1000 °C (17). Comparison of the excitation spectra for pyrochlores indicates that Eu-doped materials with high energy charge transfer states also exhibit high quenching temperatures. The reason is that high-energy charge transfer states provide a high “bridge” for energy to transition to higher levels of the intermittent ^5D_J states.

The design of phosphor materials for high-temperature thermometry should exploit

the relative positions of the energy states. The results presented in this work have shown that high energy states, such as the charge transfer state or the *d*-orbitals, play a key role in the thermal quenching properties of materials. For Ce-doped materials, our results indicate that materials which cause the splitting of the *d*-orbitals to increase will cause the emission from the $d_1 \rightarrow 4f$ transition to thermally quench at higher temperatures. For example, materials which substitute large atoms on the A-site of the garnet lattice, such as Gd^{3+} or La^{3+} , exhibit a red-shift in the Ce^{3+} emission, which indicates that the *d*-orbital splitting has increased. These materials may prove to have higher quenching temperatures. The $^5D_0 \rightarrow 4f$ emission line of Eu^{3+} is dependent on the location of the charge transfer state. We suggest that the reason higher quenching temperature are observed in materials such as $YBO_3 : Eu$ and the pyrochlores studied by (17) is because these materials have high-energy charge transfer states. Tuning Eu^{3+} materials to maximize the energy of the charge transfer state may improve thermal quenching properties of thermographic phosphors.

BIBLIOGRAPHY

[1] G. Sarner, M. Richter, and M. Alden, "Two-dimensional thermometry using temperature-induced line shifts of zno:zn and zno:ga flourescence", *Optics Letters*, vol. 33, no. 12, pp. 1327, June 2008.

[2] S.W. Allison and G.T. Gillies, "Remote thermometry with thermographic phosphors: Instrumentation and applications", *Review of Scientific Instruments*, vol. 68, no. 7, pp. 2615–2650, July 1997.

[3] K.C. Bleijenberg and G Blasse, "Qmscc calculations of thermal quenching of model phosphor systems", *Journal of Solid State Chemistry*, vol. 28, pp. DOI:10.1007/s10853–009–3906–9, 1979.

[4] C.W. Struck and W.H. Fonger, "Unified model of the temperature quenching of narrow-line and broad-band emissions", *Journal of Luminescence*, vol. 10, pp. 1–30, 1975.

[5] K.H. Henderson and G.F. Imbusch, *Optical Spectroscopy of Inorganic Solids*, Oxford Clarendon Press, 1989.

[6] R.A. Hansel, S.K. Desai, S.W. Allison, A.L. Heyes, and D.G. Walker, "Emission lifetimes of europium-doped pyrochlores for phosphor thermometry", *Journal of Applied Physics*, vol. 107, no. 1, pp. 6101, 2010.

[7] R.A. Hansel, S.W. Allison, and D.G Walker, "Temperature-dependent luminescence of gallium-substituted yag:ce", *Journal of Materials Science*, vol. 45, no. 1, pp. 146, 2009.

[8] R.A. Hansel, S.W. Allison, and D.G. Walker, "Temperature-dependent luminescence of ce3+ in gallium-substituted garnets", *Applied Physics Letters*, vol. 95, pp. 114102, 2009.

[9] Inc. Capgo, "Thermocouples", www.capgo.com/Resources/Temperature, December 2009.

[10] S.W. Allison, M.R. Cates, B.W. Noel, and G.T. Gillies, "Monitoring permanent-magnet motor heating with phosphor thermometry", *IEEE Transactions on Instrumentation and Measurement*, vol. 37, no. 4, pp. 637–641, December 1988.

[11] A.L. Heyes, J.P. Feist, X. Chen, X. Mutasim, and J.R. Nicholls, "Optical nondestructive condition monitoring of thermal barrier coatings", *Journal of Engineering for Gas Turbines and Power*, vol. 130, pp. 61301–61308, Novermber 2008.

[12] Z.Y. Zhang, K.T.V. Grattan, and A.W. Palmer, "Sensitive fiber optic thermometer using cr:lisaf fluorescence for bio-medical sensing applications", *Proceedings of the 8th Optical Fiber Sensors Conference*, pp. 93–86, January 1992.

[13] H. Maurer, R. Basner, and H. Kersten, "Measuring the temperature of microparticles in plasmas", *Review of Scientific Instruments*, vol. 79, pp. 93508, September 2008.

[14] P. Rodnyi, I. Khodyuk, E. Gorokhova, S. Mikhrin, and P. Dorenbos, "Emission and excitation spectra of zno:ga and zno:ga,n ceramics", *Optics Spectroscopy*, vol. 105, no. 6, pp. 908, 2008.

[15] M.J. Weber, "Radiative and multiphonon relaxation of rare-earth ions in Y_2O_3", *Physical Review*, vol. 171, no. 2, pp. 283–291, July 1968.

[16] A.L. Heyes, "On the design of phosphors for high-temperature thermometry", *Journal of Luminescence*, vol. doi:10.1016/j.jlumin.2009.03.041, 2009.

[17] M.M. Gentleman and D.R. Clarke, "Luminescence sensing of temperature in pyrochlore zirconate materials for thermal barrier coatings", *Surface Coating Technology*, vol. 200, pp. 1264–1269, September 2005.

[18] L. Riseberg and H. Moos, "Multiphonon orbit-lattice relaxation of excited states of rare-earth ions in crystals", *Physical Review*, vol. 174, no. 2, October 1968.

[19] B.G. Yacobi and B.G. Holt, *Non-Radiative Decay of Ions and Molecules in Solids*, North-Holland Publishing Company, Amsterdam, 1979.

[20] C Manneback, "Computation of the intensities of vibrational spectra of electronic bands in diatomic molecules", *Physica*, vol. 17, pp. 1001, 1951.

[21] E.U. Condon, "Nuclear motions associated with electron transitions in diatomic molecules", *Physical Review*, vol. 32, pp. 858–872, December 1928.

[22] G. Blasse and B.C. Grabmaier, *Luminescent Materials*, Springer Verlag Berlin Heidelberg, 1994.

[23] M. Grinberg, I. Sokolska, S. Kuck, and W. Jaskolski, "Temperature dependence of the luminescence decay of cr3+ ions in litao3: Confined potential model", *Physical Review B*, vol. 60, no. 2, pp. 959, July 1999.

[24] D.R. Clarke and S.R. Phillpot, "Thermal barrier coating materials", *Materials Today*, pp. 22–29, June 2005.

[25] M. Hirayama, N. Sonoyama, A. Yamada, and R. Kanno, "Relationship between structural characteristics and photoluminescent properties of (la1-xeux)m2o7 (m=zr, hf, sn) pyrochlores", *Journal of Luminescence*, vol. 83, pp. 1819–1825, 2008.

[26] H. Lehmann, D. Pitzer, G. Pracht, R. Vassen, and D. Stover, "Thermal conductivity and thermal expansion coefficients of the lanthanum rare-earth-element zirconate system", *Journal of the American Ceramic Society*, vol. 86, no. 8, pp. 1338–1344, August 2003.

[27] B.G. Yacobi and B.G. Holt, *Cathodoluminescence Microspy of Inorganic Solids*, Plenum Press, New York, 1990.

[28] R.D. Lumpkin, "On the design of phosphors for high-temperature thermometry", *Journal of Physics Condensed Mater*, vol. 16, pp. 8557, 2004.

[29] L.J. Tian, Y.J. Sun, Y. Yu, X.G. Kong, and H. Zhang, "Surface effect of nano-phosphors studied by time-resolved spectroscopy of ce3+", *Chemical Physics Letters*, vol. 452, pp. 188, December 2008.

[30] Y. Zhou, J. Lin, S. Wang, and H. Zhang, "Preparation of y3al5o12:eu phosphors by citricgel method and their luminescent properties", *Optical Materials*, vol. 20, pp. 13–20, 2002.

[31] A. Rabhiou, A. Kempf, and A.L. Heyes, "Examination of eu-doped thermographic phosphors for surface temperature measurements", *Proceedings of the European Combustion Meeting 2009*, pp. 859–863, 2009.

[32] Q. Dong, Y. Wang, Z. Wang, X. Yu, and Liu. B., "Self-purification-dependent unique photoluminescence properties of ybo3:eu3+ nanophosphors under vuv excitation", *Journal of Physical Chemistry C*, vol. 114, pp. 9245–9250, 2010.

[33] J. Costantini, F. Beuneu, D. Gourier, C. Trautmann, G. Calas, and M. Toulemonde, "Colour centre production in yttria-stabalized zirconia by swift charged particle irradiations", *Journal of Physics: Condensed Matter*, vol. 16, pp. 3957–3971, February 2004.

[34] S.W. Allison, G.T. Gillies, J. Rondinone, and M.R. Cates, "Nanoscale thermometry vie the flourescence of yag:ce phosphor particles: Measurements from 7 to 77c", *Nanotechnology*, vol. 14, pp. 859–863, 2003.

[35] J.L. Wu, G. Gundiah, and A.K. Cheetham, "Structure-property correlations in ce-doped garnet phosphors for use in solid state lighting", *Chemical Physics Letters*, vol. 441, pp. 250–254, 2007.

[36] D.J. Robbins, "The effects of crystal field and temperature on the photoluminescence excitation efficiency of ce3+ in yag", *Journal of the Electrochemical Society*, vol. 126, no. 9, pp. 1550–1555, 1979.

[37] H. Peng, H. Song, B. Chen, J. Wang, S. Lu, X. Kong, and J. Zhang, "Temperature dependence of luminescent spectra and dynamics in nanocrystalline $y_2o_3 : Eu^{3+}$", *Journal of Chemical Physics*, vol. 118, no. 7, pp. 3277–3282, February 2003.

[38] S.W. Allison, J.R. Buczyna, R. A. Hansel, D.G. Walker, and G.T. Gillies, "Temperature-dependent fluorescence decay lifetimes of the phosphor y3(al0.5ga0.5)5o12:ce 1%", *Journal of Applied Physics*, vol. 105, no. 3, February 2009.

[39] M. Kottaisamy, P. Thiyagarajan, J. Mishra, and M. Ramachandra Rao, "Color tuning of y3al5o12:ce phosphor and their blend for white leds", *Materials Research Bulletin*, vol. 43, pp. 1657–1663, 2008.

[40] M. Grinberg and W. Jaskolski, “Influence of a confinement-type lattice anharmonicity on the non-radiative processes in solids”, *Physical Review B*, vol. 55, no. 9, pp. 5581–5584, March 1997.

[41] M. Grinberg, A. Mandelis, and K. Fjeldsted, “Theory of interconfigurational nonradiative transitions in transition-metal ions in solids and application to the ti3+:al2o3 system”, *Physical Review B*, vol. 48, pp. 5935, 1993.